Article

Neuron

RIM C_2B Domains Target Presynaptic Active Zone Functions to PIP_2-Containing Membranes

Highlights

- RIM C_2B controls synaptic vesicle fusion downstream of priming and Ca^{2+} influx
- C_2B domains bind to PIP_2, and PIP_2 binding is required for RIM's role in release
- C_2B domains need to be tethered to other RIM domains to mediate vesicle fusion
- RIM C_2B domains have additional functions for enhancing release probability

Authors

Arthur P.H. de Jong, Carlos M. Roggero, Meng-Ru Ho, Man Yan Wong, Chad A. Brautigam, Josep Rizo, Pascal S. Kaeser

Correspondence

kaeser@hms.harvard.edu

In Brief

de Jong et al. demonstrate that the RIM C_2B domain is important for neurotransmitter release. RIM C_2B binds to the phospholipid PIP_2, and this interaction directs synaptic vesicle priming and Ca^{2+} influx to the PIP_2-containing plasma membrane for efficient exocytosis.

de Jong et al., 2018, Neuron *98*, 335–349
April 18, 2018
https://doi.org/10.1016/j.neuron.2018.03.011

CellPress

Neuron
Article

RIM C_2B Domains Target Presynaptic Active Zone Functions to PIP_2-Containing Membranes

Arthur P.H. de Jong,[1] Carlos M. Roggero,[2] Meng-Ru Ho,[2,3] Man Yan Wong,[1] Chad A. Brautigam,[4] Josep Rizo,[2] and Pascal S. Kaeser[1,5,*]

[1]Department of Neurobiology, Harvard Medical School, Boston, MA 02115, USA
[2]Departments of Biophysics, Biochemistry, and Pharmacology, University of Texas Southwestern Medical Center, Dallas, TX 75390, USA
[3]Institute of Biological Chemistry, Academia Sinica, Taipei, Taiwan
[4]Departments of Biophysics and Microbiology, University of Texas Southwestern Medical Center, Dallas, TX 75390, USA
[5]Lead Contact
*Correspondence: kaeser@hms.harvard.edu
https://doi.org/10.1016/j.neuron.2018.03.011

SUMMARY

Rapid and efficient synaptic vesicle fusion requires a pool of primed vesicles, the nearby tethering of Ca^{2+} channels, and the presence of the phospholipid PIP_2 in the target membrane. Although the presynaptic active zone mediates the first two requirements, it is unclear how fusion is targeted to membranes with high PIP_2 content. Here we find that the C_2B domain of the active zone scaffold RIM is critical for action potential-triggered fusion. Remarkably, the known RIM functions in vesicle priming and Ca^{2+} influx do not require RIM C_2B domains. Instead, biophysical experiments reveal that RIM C_2 domains, which lack Ca^{2+} binding, specifically bind to PIP_2. Mutational analyses establish that PIP_2 binding to RIM C_2B and its tethering to the other RIM domains are crucial for efficient exocytosis. We propose that RIM C_2B domains are constitutive PIP_2-binding modules that couple mechanisms for vesicle priming and Ca^{2+} channel tethering to PIP_2-containing target membranes.

INTRODUCTION

Information transfer between neurons is initiated by rapid fusion of synaptic vesicles in presynaptic nerve terminals. Synaptic vesicle exocytosis is restricted to the active zone, a protein complex that is tightly attached to the presynaptic membrane and that controls the fusion machinery (Südhof, 2012). The membrane fusion reaction itself is driven by a conserved molecular machinery composed of SNARE proteins and Munc18, among others (Jahn and Fasshauer, 2012). This machinery is highly homologous to those of secretory pathways in non-neuronal cells and unicellular organisms (Wickner, 2010), which operate without active zone-like scaffolds, and fusion itself is thought to occur independent of active zone proteins (Südhof, 2013).

To ensure the spatiotemporal precision of synaptic vesicle fusion, three fundamental requirements must be met. First, vesicles must undergo maturation steps to become highly fusogenic, broadly referred to as docking and priming (Kaeser and Regehr, 2017; Südhof, 2012). Second, voltage-gated Ca^{2+} channels must be anchored near fusion-ready vesicles so that local Ca^{2+} levels rise and fall quickly in response to a presynaptic action potential for rapid, synchronous fusion triggering (Eggermann et al., 2011). Third, efficient fusion relies on specific lipids, in particular the presence of phosphatidylinositol 4,5-bisphosphate (PIP_2) in the target membrane (Hay et al., 1995; Milosevic et al., 2005; Di Paolo et al., 2004). The importance of PIP_2 in fusion arises from its ability to boost presynaptic Ca^{2+} entry and the Ca^{2+} affinity of the fusion machinery (van den Bogaart et al., 2012; Suh et al., 2010). In many secretory cells, PIP_2 is not evenly distributed across membranes but restricted to the plasma membrane, where it forms small clusters (Aoyagi et al., 2005; van den Bogaart et al., 2011; Laux et al., 2000). Although the exact distribution of PIP_2 within a nerve terminal is not known, PIP_2 defines plasma membrane identity (Di Paolo and De Camilli, 2006) and is essential for synaptic vesicle exocytosis (Di Paolo et al., 2004). It is further often hypothesized that PIP_2 is clustered at the active zone (van den Bogaart et al., 2011; Lauwers et al., 2016). Hence, mechanisms that target the fusion machinery to PIP_2-containing membranes are necessary. Although a growing body of knowledge strongly supports the notion that the active zone provides molecular mechanisms for the first two requirements, it is unclear how these active zone functions are targeted to PIP_2-containing membranes.

Active zones, which are composed of RIM, RIM-BP, ELKS, Munc13, Piccolo/Bassoon, and Liprin-α (Wong et al., 2018), control the docking and priming of synaptic vesicles and the nearby anchoring of Ca^{2+} channels. RIMs recruit Ca^{2+} channels in a tripartite complex with RIM-BPs (Han et al., 2011; Hibino et al., 2002; Kaeser et al., 2011; Liu et al., 2011). This recruitment is mediated by the central RIM PDZ domain, which binds to Ca^{2+} channels, and a proline-rich PxxP motif between two C-terminal C_2 domains that binds to RIM-BPs, which, in turn, bind to Ca^{2+} channels as well (Figure 1A). Via its N-terminal zinc-finger domain, RIM activates and anchors Munc13 to control the number of docked and primed vesicles (Andrews-Zwilling et al., 2006; Augustin et al., 1999; Camacho et al., 2017; Deng et al., 2011; Han et al., 2011; Imig et al., 2014). Thus, RIM proteins have evolved as essential scaffolds that participate in these key active zone functions (Figure 1A).

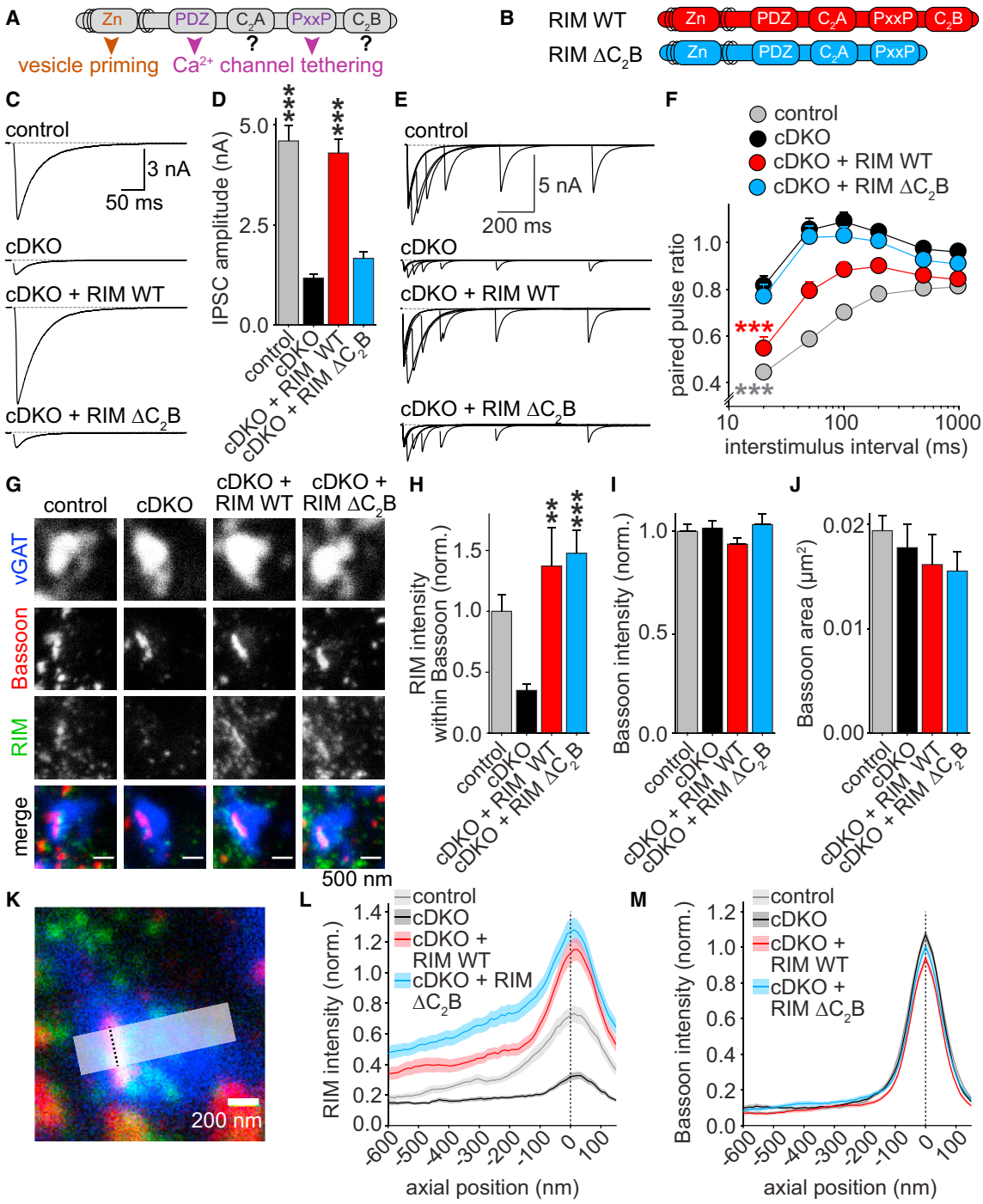

Figure 1. The RIM1 C_2B Domain Is Crucial for Synaptic Vesicle Release

(A) Domain structure of RIM1α (Zn, zinc-finger domain with surrounding α-helical regions; PxxP, proline-rich region) and key RIM functions that are assigned to specific domains.

(B) Overview of rescue proteins.

(C and D) Example traces (C) and quantification of average amplitudes (D) of single evoked IPSCs in cultured hippocampal neurons. cDKO neurons are neurons from RIM1/2 conditional knockout mice infected with a lentivirus expressing Cre recombinase, and rescue proteins were expressed from a second, independent lentivirus. Control neurons are neurons from the same culture infected with a virus expressing truncated, inactive cre. Control, n = 6 independent cultures/30 cells; cDKO, 6/30; cDKO + RIM WT, 6/31; cDKO + RIM ΔC_2B, 6/32.

(E and F) Example traces (E) and average IPSC PPRs (F) at various interstimulus intervals. Control, n = 4 independent cultures/21 cells; cDKO, 4/18; cDKO + RIM WT, 4/21; cDKO + RIM ΔC_2B, 4/21. ***p < 0.001 genotype versus cDKO by two-way ANOVA.

(legend continued on next page)

The two RIM C_2 domains, termed C_2A and C_2B, remain poorly understood despite being highly conserved across RIM proteins (Wang and Südhof, 2003). C_2 domains are widely known as Ca^{2+} sensors (Südhof, 2013), but RIM C_2 domains cannot bind Ca^{2+} (Dai et al., 2005; Guan et al., 2007). Several interactors for RIM C_2A or C_2B have been identified *in vitro*. These include Liprin-α, SNAREs, Ca^{2+} channel β subunits, and synaptotagmins (Coppola et al., 2001; Kaeser et al., 2012; Kiyonaka et al., 2007; Schoch et al., 2002), and RIM C_2B domains also dimerize (Guan et al., 2007), but the physiological relevance of these interactions at synapses remains unclear. In *C. elegans*, removal of the C_2B domain leads to a behavioral phenotype similar to RIM-null mutants (Koushika et al., 2001). Together with the high conservation, this finding suggests important roles for RIM C_2B, but it is unknown whether this is due to defects in expression and localization of RIM or due to a more direct role in synaptic transmission. Notably, RIM C_2B contains a lysine-rich polybasic stretch with high homology to several other C_2 domains (Corbalan-Garcia and Gómez-Fernández, 2014). In such C_2 domains, this motif binds to PIP_2 (Bai et al., 2004; Coudevylle et al., 2008; Guerrero-Valero et al., 2009), and mutations in this motif lead to biochemical defects and impaired synaptic transmission (van den Bogaart et al., 2012; Groffen et al., 2010; Li et al., 2006).

Given the central scaffolding role for RIM at the active zone, constitutive binding of its C_2 domains to PIP_2 could provide an attractive mechanism to target synaptic vesicle docking, priming, and Ca^{2+} channel tethering to PIP_2-containing membranes. Here we tested this hypothesis and found that both RIM C_2 domains bind PIP_2. Deleting the RIM C_2B domain or disrupting PIP_2 binding to the RIM C_2B domain strongly impaired synaptic transmission, whereas similar manipulations of the RIM C_2A domain did not have strong functional effects. Remarkably, although binding of the C_2B domain to PIP_2 was required for rescue of action potential-triggered vesicle fusion, removing C_2B did not impair the known RIM functions in vesicle priming and Ca^{2+} influx. Finally, RIM C_2B domains were inactive unless they were attached to the N-terminal RIM domains. We propose that RIM C_2B domains tether essential active zone functions to PIP_2-containing membranes for rapid and efficient exocytosis.

RESULTS

The RIM C_2B Domain Is Important for Neurotransmitter Release

Based on the high conservation of the RIM C_2B domain (Wang and Südhof, 2003), the strong behavioral defects upon RIM C_2B deletion in *C. elegans* (Koushika et al., 2001), and the general importance of C_2 domains in vesicle fusion (Südhof, 2013), we hypothesized that RIM C_2B is critical for synaptic vesicle release. To test this hypothesis, we expressed full-length wild-type RIM1α (RIM WT) and a RIM1 mutant lacking the C_2B domain (RIM ΔC_2B) in cultured hippocampal neurons obtained from RIM1/2 conditional knockout mice (Figure 1B). In this preparation, the *Rims1* and *Rims2* genes contain essential exons flanked by *loxp* sites, and we expressed Cre recombinase from a lentivirus to remove all RIM1 and RIM2 isoforms (conditional double knockout [cDKO]) (Kaeser et al., 2008, 2011). Control neurons are neurons from the same litter infected with a lentivirus that express an inactivated variant of Cre recombinase (Kaeser et al., 2008). We delivered RIM using separate lentiviruses because bicistronic expression of Cre and rescue proteins, as described before (Kaeser et al., 2011), is impractical for full-length RIM1α because of the packaging size limit of lentiviruses. This approach yielded reliable removal of endogenous RIM, and exogenous RIM expression reached levels above wild-type control neurons (Figure S1B). RIM WT expression fully rescued the amplitude of action potential evoked γ-aminobutyric acid (GABA)-ergic inhibitory postsynaptic currents (IPSCs) and nearly completely restored paired pulse ratios (PPRs) (Figures 1C–1F), which are inversely correlated with vesicular release probability (*p*) (Zucker and Regehr, 2002). RIM ΔC_2B was expressed at levels comparable with RIM WT (Figure S1B) but showed no significant increase in IPSC amplitude compared with cDKO neurons (Figures 1C and 1D). Furthermore, the PPR of RIM ΔC_2B was indistinguishable from cDKO at all intervals tested (Figures 1E and 1F). Thus, the RIM C_2B domain is necessary to enhance *p*, and removing C_2B abolishes rescue activity. Importantly, expression of RIM WT or RIM ΔC_2B in wild-type neurons did not enhance or suppress release (Figures S1C–S1H), indicating that the effects in the rescue conditions are not due to overexpression or dominant-negative roles. Furthermore, using the same experimental design, we found that deletion of RIM C_2A has no strong effect on synaptic transmission (Figures S1I–S1P). We conclude that the C_2B domain of RIM1 is crucial to set *p* at inhibitory synapses.

RIM C_2B Is Not Necessary for Localizing RIM to the Active Zone

We hypothesized that the severe phenotype of RIM ΔC_2B rescue might be due to perturbed recruitment of RIM ΔC_2B to the active zone. To test this hypothesis, we performed stimulated emission depletion (STED) microscopy on cultured neurons stained for the inhibitory synapse marker vGAT, the active zone marker Bassoon, and RIM (Figures 1G–1M and S2A). RIM signals in control synapses co-localized well with Bassoon. To measure RIM

(G–J) Example images (G) and quantification (H–J) of synapses using STED microscopy. Average RIM intensity within Bassoon objects (H), average Bassoon intensity within Bassoon objects (I), and average surface area of Bassoon objects (J) are shown. Control, n = 3 independent cultures/10 fields of view (23.5 μm × 23.5 μm, typically containing 100–300 Bassoon objects per field of view); cDKO, 3/7; cDKO + RIM WT, 3/8; cDKO + RIM ΔC_2B, 3/11.

(K–M) Schematic representation (K) and intensity profile analysis (L and M) of side view synapses. The shaded area represents the region of interest (ROI), and the dotted line indicates distance = 0 nm centered to the peak of Bassoon labeling. Average intensity profiles of RIM (L) and Bassoon (M) are shown. Data are shown as mean (solid line) ± SEM (shaded area). Control, n = 3 independent cultures/67 ROIs; cDKO, 3/72; cDKO + RIM WT, 3/83; cDKO + RIM ΔC_2B, 3/87.

All data are mean ± SEM, $^*p < 0.05$, $^{**}p < 0.01$, $^{***}p < 0.001$, analyzed by one-way ANOVA (Kruskal-Wallis test; D and H–J) unless otherwise noted; all comparisons with cDKO. For assessment of synaptic transmission upon expression of RIM WT and RIM ΔC_2B in wild-type neurons and analysis of RIM ΔC_2A rescue, see Figure S1. For STED overview images, see Figure S2A.

levels at active zones, we detected Bassoon objects within vGAT-positive synapses and measured RIM staining intensities within Bassoon objects. Although RIM rescue levels appeared to be slightly higher than control levels, we observed no difference between RIM WT and RIM ΔC_2B (Figure 1H). In addition, no differences were found in the average Bassoon intensity or the size of Bassoon objects (Figures 1I and 1J). To evaluate whether RIM ΔC_2B localized normally within the presynaptic terminal, we selected synapses in side view, defined as a cluster of vGAT-positive vesicles that contains an elongated band of Bassoon at the edge of the vGAT signal (Wong et al., 2018). We then measured the staining intensity profile along a 250-nm-wide rectangle perpendicular to the Bassoon band (Figure 1K) and aligned all profiles to the peak Bassoon intensity. Peak intensity of RIM co-localized well with Bassoon in control neurons, and peak intensity of RIM WT and RIM ΔC_2B rescue proteins, although higher in intensity than endogenous RIM, did not shift relative to Bassoon (Figure 1L). The Bassoon signal did not change across conditions (Figure 1M). Despite complete absence of RIM in western blotting (Figure S1B; Kaeser et al., 2011), a small peak remained in cDKO in STED, similar to the 25% background with the same antibody in confocal analyses (Wang et al., 2016). These data establish that the RIM C_2B domain is not required for RIM active zone localization.

The RIM C_2B Domain Mediates a New Function of RIM

We next assessed whether the RIM C_2B domain participates in the two established RIM functions, which are synaptic vesicle priming via recruitment of Munc13 (Andrews-Zwilling et al., 2006; Camacho et al., 2017; Deng et al., 2011) and enhancing Ca^{2+} influx by tethering of presynaptic Ca^{2+} channels (Han et al., 2011; Kaeser et al., 2011; Müller et al., 2012). To test whether RIM C_2B is required to recruit Munc13 to the active zone, we quantified Munc13 levels within Bassoon objects using STED microscopy (Figures 2A–2D and S2B–S2D). RIM cDKO led to a reduction in Munc13 at the active zone, consistent with the reduction of Munc13 in RIM cDKO neurons (Deng et al., 2011). Strikingly, RIM ΔC_2B and RIM WT rescue led to Munc13 levels slightly above control levels (Figure 2B), and the Munc13 peak intensity localized to the active zone under control as well as rescue conditions (Figure 2C). We next measured the size of the primed vesicle pool (readily releasable pool [RRP]) by application of hypertonic sucrose (Rosenmund and Stevens, 1996) and observed that RIM WT and RIM ΔC_2B rescued RRP size to similar levels (Figures 2E and 2F). Thus, despite the failure to rescue action potential-induced release, RIM ΔC_2B is able to recruit Munc13 to active zones and to restore the RRP.

To test whether the RIM C_2B domain contributes to presynaptic Ca^{2+} influx, we loaded individual cells with the low-affinity Ca^{2+} indicator Fluo-5F through a patch pipette and measured Ca^{2+} influx in individual presynaptic boutons in response to a single action potential induced by a brief somatic current injection (Figures 2G and 2H). Both RIM WT and RIM ΔC_2B significantly increased presynaptic Ca^{2+} influx compared with cDKO, and no difference was observed between the two rescue conditions. Thus, the C_2B domain is not required to boost presynaptic Ca^{2+} influx. Taken together, these data establish that the RIM C_2B domain is critical to enhance p, but it does so independent of the known roles of RIM in vesicle priming or Ca^{2+} influx.

RIM C_2 Domains Bind to PIP_2

What is the function of RIM C_2B domains in synaptic transmission? The RIM C_2B domain contains a lysine-rich polybasic sequence that is highly conserved among C_2 domains, and this sequence mediates binding to the phospholipid PIP_2 in several other C_2 domains (reviewed in Corbalan-Garcia and Gómez-Fernández, 2014). To test whether RIM1 C_2B binds to PIP_2, we performed liposome binding assays in which we measured co-sedimentation of purified C_2B with heavy liposomes (Figures 3A and 3B). Although we detected only weak binding of C_2B to liposomes composed of phosphatidylcholine (PC) and phosphatidylserine (PS), addition of PIP_2 enhanced co-sedimentation of the C_2B domain with liposomes, suggesting direct binding of C_2B to PIP_2. Changing the surface charge of the liposomes by adding extra PS did not alter the amount of binding, suggesting that the interaction is specific for PIP_2 and not simply mediated by changes in membrane charge (Figures 3A and 3B). We then tested how different lipid compositions of the liposomes influenced binding of the RIM C_2B domain using co-floatation assays. We found that the binding was almost entirely specific for PIP_2 (Figure 3C), and other lipids, including the phosphoinositides PI and PIP, only showed weak binding.

We next used nuclear magnetic resonance (NMR) spectroscopy and a water-soluble PIP_2 analog (dibutanoyl phosphatidylinositol 4,5-bisphosphate [diC4-PIP_2]) to characterize its interaction with the RIM1 C_2B domain. ^1H-^{15}N heteronuclear single quantum coherence (HSQC) spectra of C_2B in the absence and presence of 100 μM diC4-PIP_2 revealed specific cross-peak shifts (Figure 3D), demonstrating a direct interaction. To measure the binding affinity, we repeated the experiment at increasing concentrations of diC4-PIP_2 (0–250 μM), which resulted in progressive shifts of the same cross-peaks (Figure 3E). We fitted the perturbations of individual chemical shifts from the cross-peaks that were most affected by diC4-PIP_2 binding as a function of diC4-PIP_2 concentration and obtained K_D values that ranged from 32 to 79 μM (Figure 3F). The K_D values are within the range of those found for other C_2 domains (van den Bogaart et al., 2012; Montaville et al., 2008), and the variability is expected, considering that some shifts are relatively small. These results establish RIM1 C_2B as a PIP_2 binding module.

It was previously suggested that C_2B forms a weak dimer via an interface that partly overlaps with the polybasic sequence (Guan et al., 2007), which, thus, might interfere with PIP_2 binding. Using analytical ultracentrifugation, we found that the C_2B homodimer affinity was very weak (K_D ~3 mM; Figure 3G), which makes it very unlikely to be physiologically relevant. Additionally, we found that the addition of PIP_2 did not change the line widths of methyl resonances of 1D ^1H-NMR spectra of RIM1 C_2B, indicating that PIP_2 does not change the very weak dimerization of C_2B (Figure 3H).

We finally characterized the PIP_2 binding of RIM1 by analyzing its C_2A domain with the same assays (Figures S3A–S3F). We observed a specific interaction of C_2A with PIP_2-containing liposomes, and titrations monitored by ^1H-^{15}N HSQC spectra yielded a K_D value that was comparable with those measured

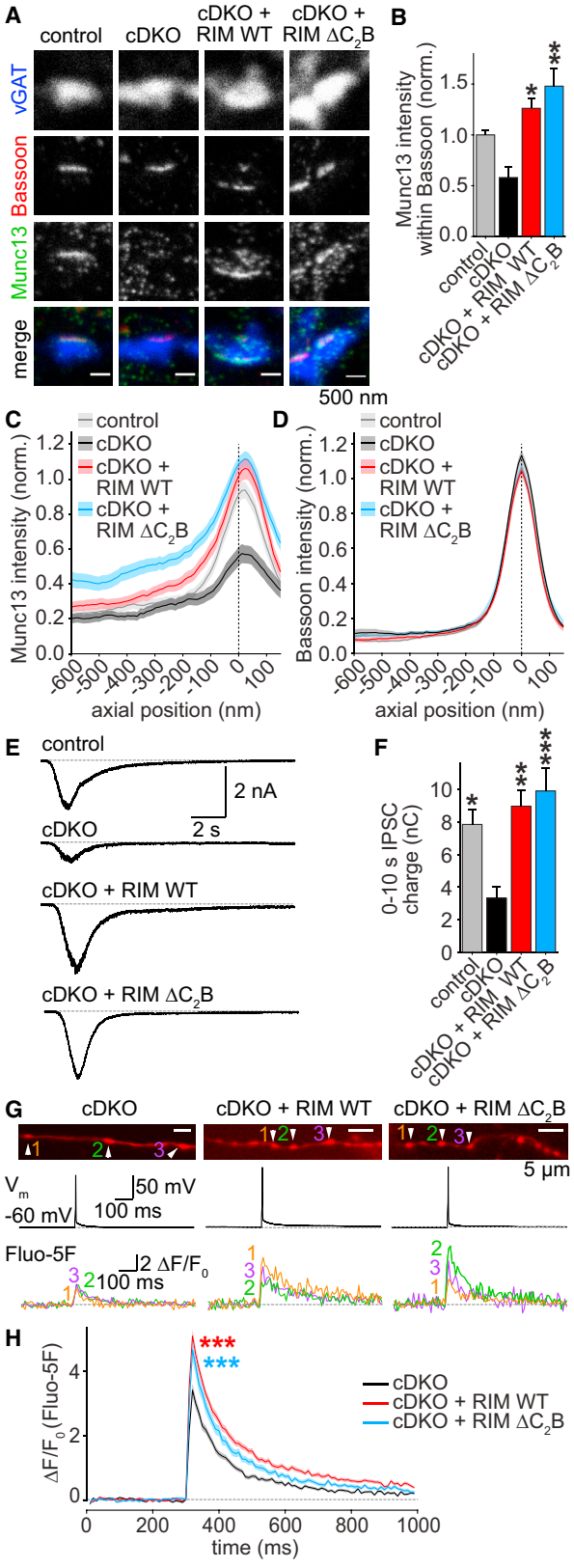

Figure 2. RIM1 C_2B Domains Are Dispensable for the Functions of RIM in Munc13 Recruitment, Vesicle Priming, and Ca^{2+} Influx

(A and B) Example images (A) and average Munc13 intensity (B) of synapses in STED microscopy. Control, n = 3 independent cultures/7 fields of view; cDKO, 3/6; cDKO + RIM WT, 3/6; cDKO + RIM ΔC_2B, 3/6.

(C and D) Intensity profile for Munc13 (C) and Bassoon (D) in side view synapses. Control, n = 3 independent cultures/60 ROIs; cDKO, 3/53; cDKO + RIM WT, 3/64; cDKO + RIM ΔC_2B, 3/66.

(E and F) Example traces (E) and quantification of IPSC charge (F) integrated over 10 s, induced by a focal 10-s puff of hyperosmolar sucrose (500 mM) as a measurement of the RRP. Control, n = 3 independent cultures/13 cells; cDKO, 3/15; cDKO + RIM WT, 3/13; cDKO + RIM ΔC_2B, 3/13.

(G and H) Example boutons (G) and quantification (H) of presynaptic Ca^{2+} imaging. Individual cells were filled with Alexa 647 and the Ca^{2+} indicator Fluo-5F through a patch pipette. In (G), images of Alexa 647 fluorescence in axons (top), the somatic membrane potentials (center), and Fluo-5F fluorescence traces of individual boutons during a single action potential (bottom) in response to a brief somatic current injection are shown. Arrowheads in Alexa 647 images indicate the boutons from which the Fluo-5F signals at the bottom were obtained. (H) shows the average Fluo-5F $\Delta F/F_0$ during a single action potential, where ΔF is the change in fluorescence in response to an action potential and F_0 is the baseline fluorescence before the action potential. cDKO, n = 3 independent cultures/8 cells/153 boutons; cDKO + RIM WT, 3/8/160; cDKO + RIM ΔC_2B, 3/8/93. ***p < 0.001 genotype versus cDKO by 2-way ANOVA for the first 6 frames after stimulation.

All data are mean ± SEM, *p < 0.05, **p < 0.01, ***p < 0.001 versus cDKO analyzed by one-way ANOVA (Kruskal-Wallis test, B and F) unless otherwise noted; all comparisons with cDKO. For overview STED images and quantification of Bassoon signals, see Figures S2B–S2D.

for C_2B. Thus, RIM1 can bind to PIP_2-containing membranes via its C_2A and C_2B domains.

Distinct PIP_2 Binding Modes of the RIM C_2 Domains

We next designed mutations to interfere with PIP_2 binding. Because RIM1 C_2B contains a polybasic sequence that is conserved among PIP_2-binding C_2 domains (Figure S3G), we based our mutations on homologous PIP_2-binding sequences (Corbalan-Garcia and Gómez-Fernández, 2014). Using lipid co-sedimentation, we found that mutating single or multiple lysine (K) residues to glutamates (E) in the conserved polybasic sequence strongly impaired PIP_2 binding (Figures 4A and 4B). From these mutants, we selected a double mutant in which K1513 and 1515 were mutated to E (K1513/1515E, named C_2B 2E from hereon) for further analysis because these lysines are conserved and have been well characterized in homologous C_2 domains in biochemical and functional assays (Figures 4C and 4D; van den Bogaart et al., 2012; Groffen et al., 2010; Guerrero-Valero et al., 2009; Li et al., 2006). The ^1H-^{15}N HSQC spectrum of C_2B 2E exhibited only small perturbations compared with that of WT C_2B (Figure 4E), showing that the mutation did not perturb the folding of the domain. Importantly, no cross peak shifts were observed after the addition of diC4-PIP_2 in RIM1 C_2B 2E (Figure 4F), demonstrating that the 2E mutation abolished PIP_2 binding.

The polybasic sequence is only partially conserved in RIM1 C_2A (Figure S3G). When we tested whether the lysine and arginine (K809 and R811) residues in C_2A, at corresponding positions to K1513 and K1515 in C_2B, were necessary for PIP_2 binding of C_2A, we found that mutating them to glutamates (KR mutant) did not completely abolish diC4-PIP_2 binding

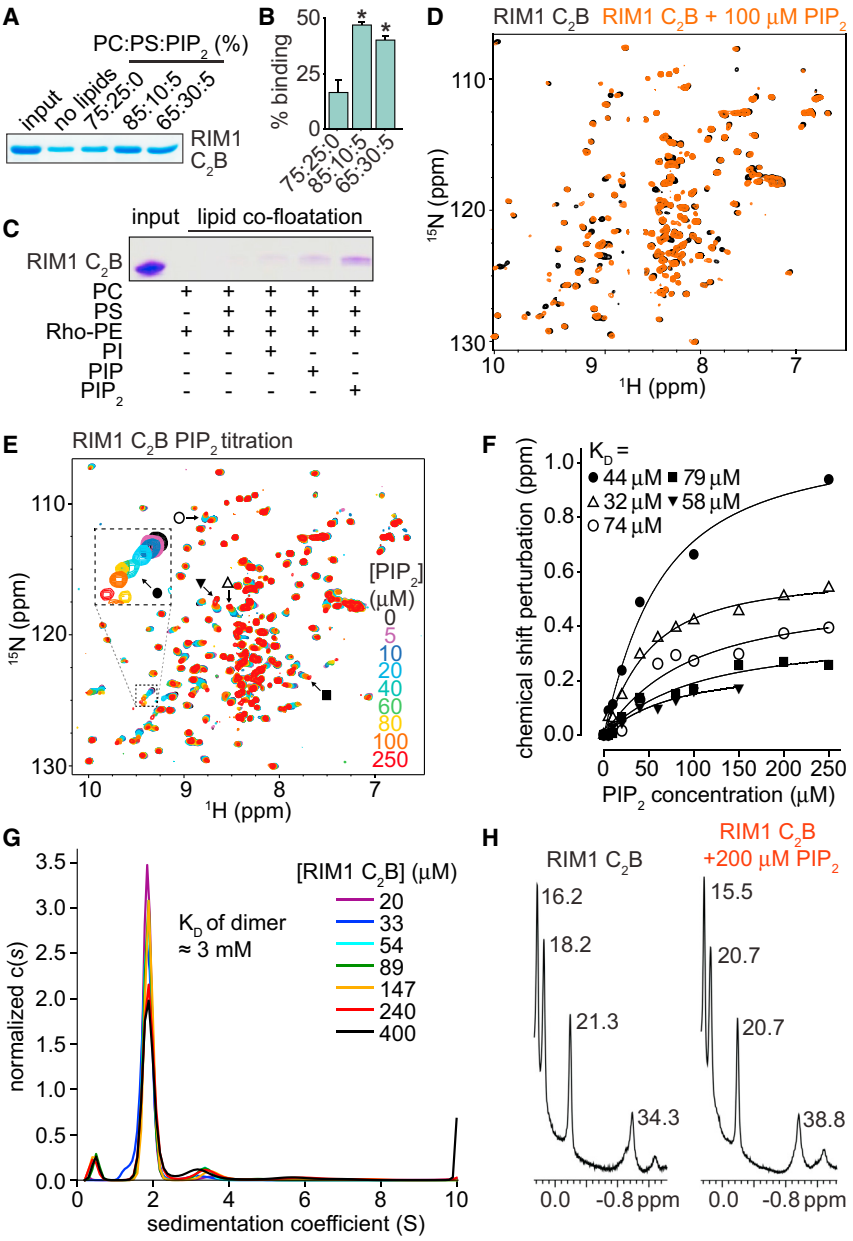

Figure 3. RIM1 C_2B Domains Bind Specifically to the Phospholipid PIP_2

(A and B) Example Coomassie-stained SDS-PAGE gel (A) and average C_2B domain content in the pellet (B) of a lipid co-sedimentation experiment using heavy liposomes of various compositions and purified His-C_2B domains. PC, phosphatidylcholine; PS, phosphatidylserine. Averages ± SEM were obtained from 3 independent experiments. Statistical significance was assessed by Student's t test, with *$p < 0.05$ versus the 75:25:0 condition.

(C) Image of a Coomassie-stained SDS-PAGE of a lipid co-floatation assay to test for PIP_2 specificity of lipid-C_2B binding. The assay was performed with purified RIM1 C_2B and various liposome compositions as indicated.

(D) Analysis of PIP_2 binding to RIM1 C_2B using NMR spectroscopy. Superposition of ^1H-^{15}N HSQC spectra of ^{15}N-labeled RIM1 C_2B alone (black contours) and in the presence of 100 µM diC4-PIP_2 (orange contours), a water-soluble PIP_2 analog.

(E) Superposition of ^1H-^{15}N HSQC spectra of RIM1 C_2B acquired in the presence of different diC4-PIP_2 concentrations as indicated by the color code. Symbols indicate cross-peak shifts for which the dissociation constants (K_D) in (F) were calculated.

(F) Analysis of the binding affinity of PIP_2 to ^{15}N-labeled RIM1 C_2B using NMR spectroscopy. Shown are plots of ^{15}N chemical shift perturbations (corresponding to labels in E) as a function of diC4-PIP_2 concentration for selected cross-peaks. The data for each cross-peak were fitted with a standard single-site binding model, yielding the K_D per cross-peak.

(G) Analytical ultracentrifugation of RIM1 C_2B at various concentrations. The *c*(*s*) distributions shown were normalized to the total signal in each distribution. The K_D of the dimer is indicated.

(H) Expansions showing the well-resolved methyl resonances of 1D ^1H-NMR spectra of RIM1 C_2B alone (left) and in the presence of 200 µM diC4-PIP_2 (right). The line widths (in hertz) are indicated next to each resonance and are comparable in the two spectra.

For experiments assessing PIP_2 binding of RIM1 C_2A, see Figure S3.

(Figures S4A and S4B). Instead, RIM1 and RIM2 C_2A contain two unique arginines at the bottom of the β sandwich (R834 and R835; Figures S3G and S4A) that could potentially bind to PIP_2, and mutation of one of these arginines has been associated with autosomal cone-rod dystrophy in human genetic studies (Johnson et al., 2003). ^1H-^{15}N HSQC spectra showed that mutation of both arginines to glutamate (C_2A 2E mutant) abolished binding of RIM1 C_2A to diC4-PIP_2 without perturbing its folding (Figures S4C and S4D). Hence, RIM1 C_2 domains, and likely other C_2 domains, can bind to PIP_2 through different motifs located at distinct regions of the β sandwich.

Finally, we tested whether the binding of the RIM C_2 domains to phosphoinositides is restricted to PIP_2 phosphorylated at the 4 and 5 positions at the inositol ring ($PI(4,5)P_2$). We found that isomers other than $PI(4,5)P_2$, as well as phosphatidylinositol 3,4,5-triphosphate (PIP_3), induced only weak or no binding of C_2B to liposomes in lipid co-sedimentation assays (Figures S4E–S4H). Hence, phosphoinositide binding of RIM C_2B is mostly specific for $PI(4,5)P_2$. Importantly, the 2E mutation of either C_2A or C_2B inhibited binding to all PIP_2 isomers.

The Polybasic Region of RIM C_2B Is Critical for Synaptic Vesicle Release

To investigate the functional importance of the interactions of RIM C_2 domains with PIP_2, we generated a RIM1 mutant that harbors the 2E mutations of both C_2A and C_2B (RIM 4E; Figure 5A). RIM 4E was expressed at levels comparable with RIM WT, was efficiently recruited to synapses, and restored the

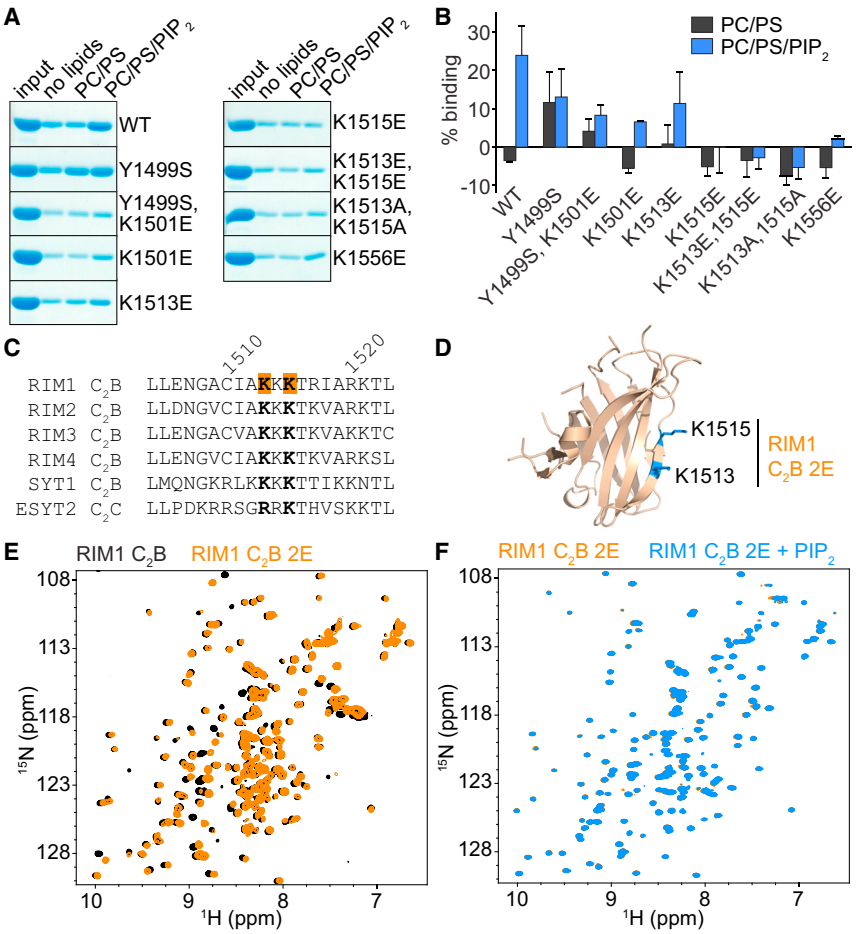

Figure 4. Mutations in the Polybasic Sequence of RIM1 C_2B Abolish PIP_2 Binding

(A and B) Example gels (A) and quantification (B) of liposome co-sedimentation assays using His-C_2B domains. Binding was quantified as percent of total input, and the signal in the no lipids sample was set to 0% for normalization. Data are shown as mean ± SEM from 3 independent experiments. Liposome composition (PC:PS:PIP_2):PC/PS, 65:35:0: PC:PS:PIP_2, 65:30:5.

(C) Sequence alignment (see also Figure S3G) of the polybasic sequence of the C_2B domains of rat RIM1 (Uniprot: Q9JIR4), RIM2 (Uniprot: Q9JIS1), RIM3 (Uniprot: Q9JIR3), RIM4 (Uniprot: Q8CIX1), synaptotagmin-1 (SYT1, Uniprot: P21707), and human extended synaptotagmin 2 (ESYT2, Uniprot: A0FGR8). The lysine residues mutated in RIM1 C_2B 2E are highlighted in orange. Conservation of mutated lysines is shown in bold. Numbers on top indicate residue positions in RIM1.

(D) Ribbon diagram of the RIM1 C_2B domain showing the locations of the mutated residues (PDB: 2Q3X; Guan et al., 2007).

(E) Superposition of ^1H-^{15}N HSQC spectra of ^{15}N-labeled RIM1 C_2B WT (black contours) and RIM1 C_2B 2E (orange contours) domains.

(F) Analysis of PIP_2 binding to ^{15}N-labeled RIM1 C_2B 2E using NMR spectroscopy. Shown is superposition of ^1H-^{15}N HSQC spectra of RIM1 C_2B 2E alone (orange contours) and RIM1 C_2B 2E in the presence of 100 μM diC4-PIP_2 (blue contours).

For mutational analyses of C_2A-PIP_2 binding and of binding of RIM C_2 domains to PIP_3 and various PIP_2 isomers, see Figure S4.

priming deficit of RIM cDKO (Figures S5A–S5F). The amplitude of evoked IPSCs, however, was severely reduced compared with control and RIM WT rescued cells and was statistically indistinguishable from that of cDKO neurons (Figures 5A–5C). In addition, RIM 4E showed no rescue of PPRs (Figures 5D and S5G) or release induced by brief action potential trains (10 action potentials at 10 Hz; Figures S5H and S5I). Thus, the RIM 4E mutant did not rescue *p* and phenocopied the RIM ΔC_2B rescue experiments (Figures 1 and 2).

To test whether the phenotype of RIM 4E is due to mutations in C_2A, C_2B, or both, we generated variants of RIM in which only C_2A (RIM A2E) or C_2B (RIM B2E) was mutated (Figure 5E). As observed with RIM 4E, RIM A2E or B2E mutants expressed normally (Figure S5J). Although RIM A2E led to significant rescue of the IPSC amplitude, RIM B2E did not show any rescue (Figures 5F and 5G). Similarly, RIM A2E rescued PPRs as efficiently as RIM WT, but RIM B2E did not display any rescue at all (Figure 5H and Figure S5K). Thus, we could not detect a statistically significant defect in synaptic transmission upon abolishing PIP_2 binding to C_2A, consistent with the finding that removing the C_2A domain does not impair rescue (Figures S1H–S1P). However, mutating the polybasic region in RIM C_2B alone leads to absence of rescue. This establishes a central role for this motif in synaptic vesicle fusion.

Known Protein Interactions of RIM C_2B Do Not Mediate Its Role in Exocytosis

Is the effect of the C_2B 2E mutation solely due to a loss of PIP_2 binding or does the mutation affect other molecular interactions as well? Previous studies have proposed that multiple proteins interact with RIM1 C_2B, including Liprin-α (Schoch et al., 2002), synaptotagmin-1 (Coppola et al., 2001; Schoch et al., 2002), the SNARE proteins syntaxin-1 and SNAP-25 (Coppola et al., 2001), and β subunits of Ca^{2+} channels ($Ca_V\beta$; Kiyonaka et al., 2007), although several of these interactions could not be reproduced by NMR spectroscopy (Guan et al., 2007). To test whether C_2B 2E mutations interfere with these interactions, we performed glutathione S-transferase (GST) affinity purifications from mouse brain and detected potential interactors by western blotting. We could not detect any binding to SNAREs and $Ca_V\beta4$ (Figure 6A). To further characterize potential binding to SNAREs, we acquired ^1H-^{15}N HSQC NMR spectra of ^{15}N-labeled C_2B WT without or with unlabeled syntaxin-1 or SNAP-25 (Figures S6A and S6B). No binding between C_2B and these SNARE proteins was observed. We did observe weak Ca^{2+}-dependent binding of C_2B to synaptotagmin-1 in GST affinity purification, which was not affected in C_2B 2E (Figure S6C) and, hence, is unlikely to explain the strong impairment in exocytosis of RIM1 C_2B 2E. Furthermore, we suspect that this

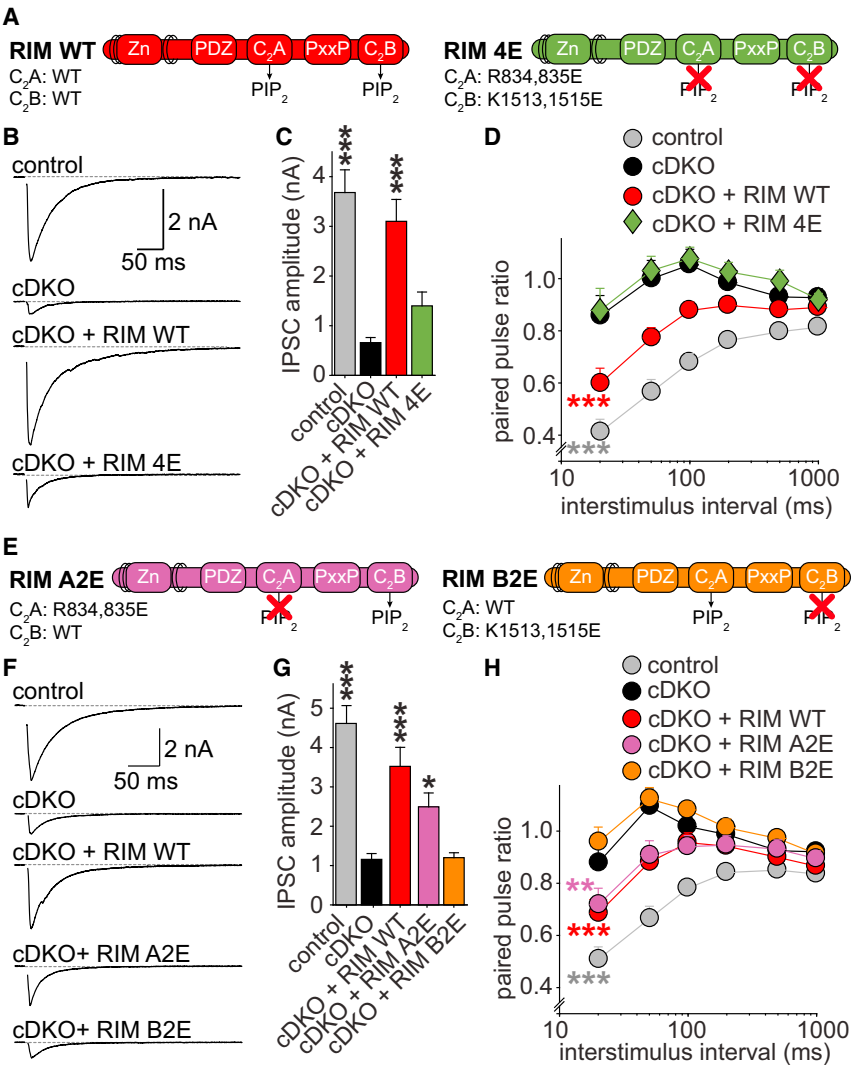

Figure 5. The PIP_2-Binding Interface of C_2B Controls Synaptic Vesicle Release

(A) Overview of rescue proteins.

(B and C) Example traces (B) and quantification of average amplitudes (C) of single evoked IPSCs. Control, n = 8 independent cultures/34 cells; cDKO, 8/32; cDKO + RIM WT 8/39; cDKO + RIM 4E, 8/38.

(D) IPSC PPRs at various interstimulus intervals. Control, n = 3 independent cultures/11 cells; cDKO, 3/12; cDKO + RIM WT, 3/14; cDKO + RIM 4E, 3/14.

(E–H) Identical to (A)–(D) but for mutations in only the C_2A (A2E) or C_2B (B2E) domains. Control, n = 4 independent cultures/15 cells; cDKO, 4/16; cDKO + RIM WT, 4/17; cDKO + RIM A2E, 4/19; cDKO + RIM B2E, 4/19.

All data shown as mean ± SEM; $^*p < 0.05$, $^{**}p < 0.01$, $^{***}p < 0.001$ for IPSC amplitudes analyzed by one-way ANOVA (Kruskal-Wallis test; C and G); for PPRs analyzed by two-way ANOVA (D and H); all comparisons with cDKO. For expression analysis of rescue proteins, RRP measurements, example traces for PPRs, and analyses of stimulation trains, see Figure S5.

binding is largely artifactual because of polyacidic impurities upon purification of GST-RIM1 C_2B (Figures S6D and S6E), which was previously observed for synaptotagmin C_2 domains (Ubach et al., 2001). In line with this conclusion, this interaction could not be observed using purified protein preparations and NMR spectroscopy (Guan et al., 2007).

As reported previously (Schoch et al., 2002), RIM1 C_2B bound to Liprin-α in GST affinity purifications, and we found that the 2E mutation in C_2B did not impair binding (Figure 6A). While testing binding of the C_2B domains of RIM3 and RIM4, two short RIM homologs that have no known function in synaptic transmission, we found that neither bound to Liprin-α (Figure 6A). To further characterize the RIM C_2B-Liprin-α interaction, we performed affinity binding assays using the Liprin-α3 LH1 or LH2 domain fused to GST (GST-Liprin-α3-LH1 and -LH2) on beads and His-tagged C_2B variants in solution, which do not show the ribonucleic acid contaminants that lead to artifacts using GST-C_2 domains (Figures S6D and S6E). We found that RIM1 C_2B, RIM1 C_2B 2E, and RIM2 C_2B bound specifically to LH2 (Figures 6B and 6C). In contrast, neither RIM3 C_2B nor RIM4 C_2B showed any appreciable binding. Thus, the interaction of RIM1 C_2B with Liprin-α is not affected by the 2E mutation, and RIM3 and RIM4 C_2B do not bind to Liprin-α. In contrast, the polybasic sequence is fully conserved between RIM1, RIM3, and RIM4 C_2B (Figure S3G), and we found that RIM1, RIM3, and RIM4 C_2B bind to PIP_2 to a similar extent in lipid co-sedimentation experiments (Figures 6D and 6E). Thus, RIM3 and RIM4 C_2B bind to PIP_2 but not to Liprin-α.

One possible scenario for the function of RIM C_2B is that it recruits Liprin-α to PIP_2-enriched membranes and that synergistic binding to Liprin-α and PIP_2 is required to control synaptic transmission. Another scenario is that the C_2B domain does not work autonomously in synaptic transmission but tethers the biochemical activities of other RIM domains to PIP_2-containing membranes. A previous study supports the latter possibility because expression of the RIM2 C_2B domain alone did not confer rescue of synaptic transmission (Kaeser et al., 2012). To directly test whether Liprin-α binding is involved in rescue, we made use of the finding that RIM3 and RIM4 C_2B do not bind to Liprin-α but bind to PIP_2. We created hybrid constructs of RIM1 where the C_2B domain is replaced with that of RIM3 (RIM 1-3) or RIM4 (RIM 1-4) and tested their effect on synaptic transmission (Figures 6F–6I). RIM 1-3 and RIM 1-4 were expressed at levels comparable with RIM WT (Figure S7A). RIM 1-4 fully rescued evoked release as well as PPRs, indistinguishable from RIM WT rescue (Figures 6G–6I and S7B). These findings directly demonstrate that Liprin-α binding to C_2B is not required for rescue. Somewhat surprisingly, RIM 1-3, although having biochemical properties identical to RIM 1-4 in terms of PIP_2 and Liprin-α binding, showed only partial rescue of evoked release and strongly

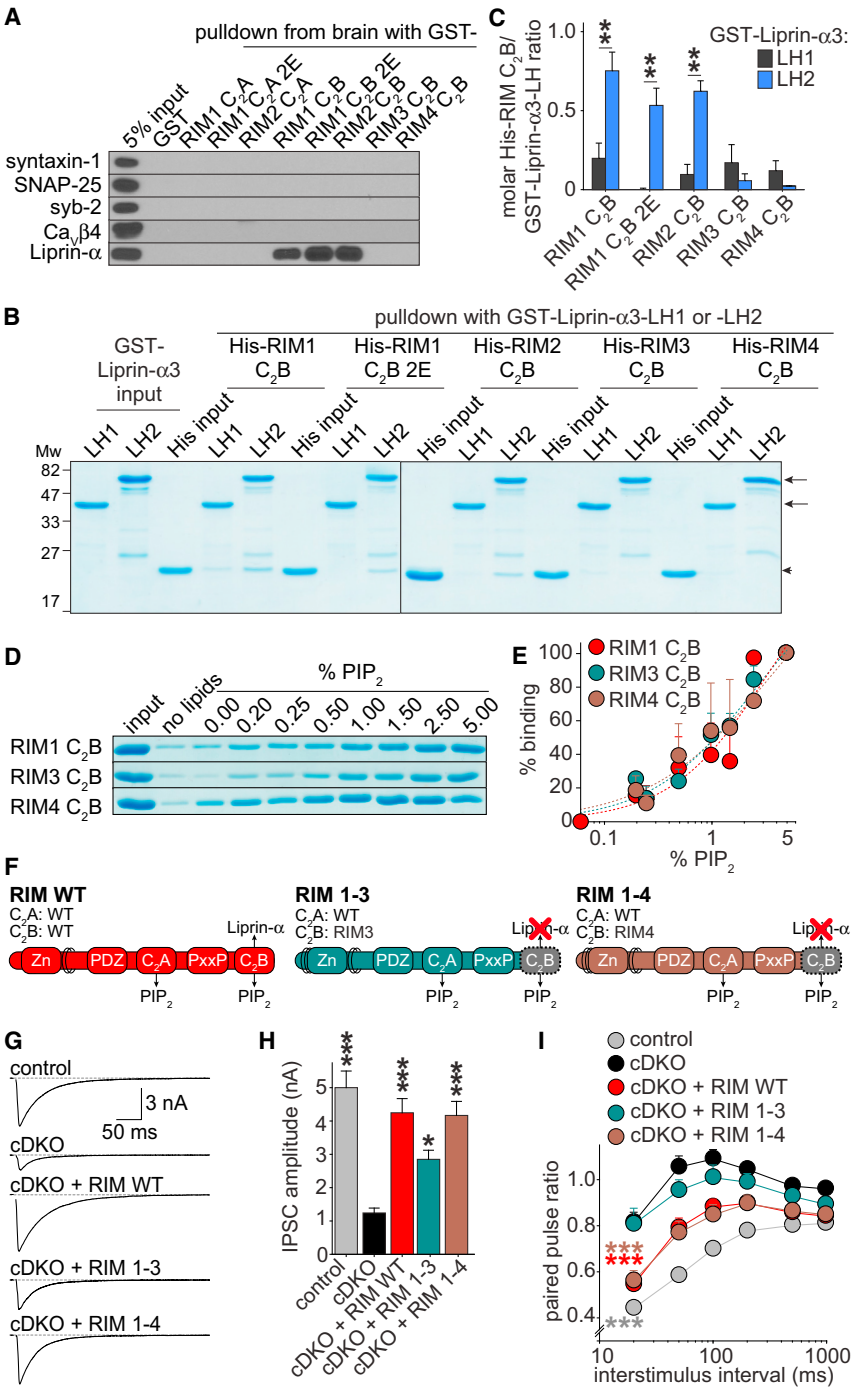

Figure 6. PIP_2 but Not Liprin-α Binding of RIM C_2B Is Required for Rescue

(A) Example images of western blots of GST affinity purifications to test for binding of RIM C_2 domains to syntaxin-1, SNAP-25, synaptobrevin/VAMP-2 (syb-2), $Ca_V\beta4$ subunits, and Liprin-α from mouse brain lysate. Each experiment was performed in at least 3 independent repeats.

(B and C) Representative gels (B) and quantification (C) of affinity binding assays with GST-Liprin-α3-LH1 and -LH2 on beads and His-tagged RIM C_2B variants in solution. Arrows in (B) indicate GST-Liprin-α3-LH1 and -LH2 bands; arrowheads indicate the His-RIM C_2B band. The average molar His-RIM C_2B/GST-Liprin-α3-LH ratio was obtained from 3 independent replicates.

(D and E) Representative gels (D) and quantification (E, average of 3 independent repeats) of lipid co-sedimentation of RIM1, RIM3, and RIM4 His-C_2B domains with heavy liposomes with increasing content of PIP_2. Liposome composition (PC:PS:PIP_2): 0% PIP_2 (65:35:0), up to 5% PIP_2 (65:30:5). The dotted line in (E) represents a Hill fit through the data points.

(F) Overview of rescue proteins.

(legend continued on next page)

diminished rescue of PPRs (Figures 6G–6I). These observations suggest that C_2B may have additional unidentified roles that are not conserved in RIM3 C_2B. To further test whether C_2B might have a second activity besides PIP_2 binding, we exchanged C_2B with another PIP_2-binding C_2 domain. The C_2C domain of extended synaptotagmin-2 has a polybasic sequence nearly identical to RIM C_2B (Figures 4C and S3G) and binds to PIP_2 but not Ca^{2+} (Giordano et al., 2013). The resulting hybrid construct (RIM ΔC_2B-C_2C; Figure S7C) was efficiently expressed in cultured neurons and rescued vesicle priming (Figures S7D–S7F) but failed to rescue evoked release as well as PPRs (Figures S7G–S7J). We conclude that RIM1 C_2B likely has an additional function in synaptic transmission or, more trivially, that artificially fusing RIM3 C_2B or extended synaptotagmin-2 C_2C with RIM1 affects the packing of the C-terminal C_2 domain against the rest of the protein, which, in turn, reduces rescue activity.

C_2B Needs to Be Attached to RIM to Mediate Rescue

Our results so far suggest that C_2B tethers previously identified functions of RIM in synaptic vesicle exocytosis to membranes that contain PIP_2. However, it is also possible that C_2B has an autonomous function at the active zone and does not need to be attached to the N-terminal RIM domains to increase synaptic vesicle fusion. To distinguish between these possibilities, we expressed RIM C_2B alone or together with RIM ΔC_2B (RIM ΔC_2B + C_2B; Figures 7A and S7K) and measured the effect on synaptic transmission. Strikingly, we observed no rescue of IPSC amplitudes or PPRs by RIM C_2B alone or by RIM ΔC_2B + C_2B; only RIM WT was sufficient for rescue (Figures 7B–7D and S7L). These results indicate that C_2B needs to be attached to the N-terminal domains of RIM to execute its role in synaptic vesicle release, directly establishing a tethering function.

RIM C_2B Has a Universal Role in Synaptic Transmission

The results discussed so far demonstrate that RIM1 C_2B has a crucial function in regulating *p* at inhibitory synapses. Is this function unique to GABAergic synaptic transmission or shared among many synapses? To address this, we recorded *N*-methyl-D-aspartate (NMDA) receptor-mediated excitatory postsynaptic currents (EPSCs) in cultured hippocampal neurons in control neurons, cDKO neurons, and cDKO neurons rescued with full-length RIM or RIM ΔC_2B. When measuring single evoked EPSC amplitudes, we found that RIM ΔC_2B did not show any rescue (Figures 7E and 7F). Additionally, RIM ΔC_2B failed to rescue PPRs (Figures 7G and S7M), indicating a defect in *p* at excitatory synapses. These results establish that the role of C_2B is not restricted to inhibitory synapses but, instead, may be important at diverse synapses throughout the brain.

DISCUSSION

The presynaptic active zone controls vesicle docking, priming, and the anchoring of Ca^{2+} channels. The fusion reaction itself is mediated by SNARE proteins (Jahn and Fasshauer, 2012; Südhof, 2013) and requires PIP_2 in the target membrane (Di Paolo et al., 2004). We found here that both C_2 domains of RIM bind to PIP_2 and that the interaction between the C_2B domain and PIP_2 is essential for RIM's role in synaptic vesicle fusion. Importantly, the C_2B domain cannot act autonomously to mediate this role but needs to be attached to the other RIM domains. In contrast to interactions of other presynaptic C_2 domain proteins with PIP_2, PIP_2 interactions of RIM are not controlled by Ca^{2+} binding to RIM C_2B and may thus fulfill constitutive, activity-independent functions. We propose that the RIM C_2B domain clusters the vesicle priming and Ca^{2+} channel tethering functions of RIM to PIP_2 in the target membrane to enable fast and efficient exocytosis (Figure 7H).

PIP_2 Binding of RIM C_2 Domains

We found that RIM1 C_2B binds specifically to PIP_2-containing membranes via a binding region that is similar to those of homologous C_2 domains (Figures 3 and 4; Corbalan-Garcia and Gómez-Fernández, 2014). Indeed, as observed previously for other PIP_2-binding C_2 domains (van den Bogaart et al., 2012; Guerrero-Valero et al., 2009; Li et al., 2006), mutations in the polybasic sequence of RIM1 C_2B (K1513E, K1515E) abolish binding to PIP_2. We further found that RIM C_2A binds to PIP_2. Surprisingly, this interaction was largely mediated by R834 and R835 located at the bottom of the β sandwich, an area that has not been implicated in PIP_2 binding of other C_2 domains. This finding suggests a new mode of PIP_2 binding that may also be employed by other C_2 domains. Although we identified essential roles for PIP_2 binding to RIM C_2B in synaptic transmission, we could not detect a strong effect of PIP_2 binding to the C_2A domain in synaptic transmission at hippocampal synapses. It is interesting, however, that a point mutation in R834 is associated with cone-rod dystrophy 7 (CORD7), a form of late-onset blindness (Johnson et al., 2003). Thus, the C_2A-PIP_2 interaction may play important roles that are either too mild to detect in our experimental paradigm, act on processes not tested here, or may be more pronounced in other synapses.

RIM C_2B Is Critical for Action Potential-Mediated Release

RIM ΔC_2B did not rescue action potential-evoked vesicle release in RIM cDKO, demonstrating that C_2B is essential for the function of RIM in synaptic transmission (Figures 1 and 2). This is in line with a study in *C. elegans*, where ΔC_2B phenocopies behavioral impairments caused by deletion of RIM (Koushika et al., 2001).

(G and H) Example traces (G) and quantification of average amplitudes (H) of single evoked IPSCs. Control, n = 4 independent cultures/21 cells; cDKO, 4/21; cDKO + RIM WT, 4/22; cDKO + RIM 1-3, 3/16; cDKO + RIM 1-4, 4/21.

(I) IPSC PPRs at various interstimulus intervals. The number of observations is as in (H).

All data are shown as mean ± SEM; *p < 0.05, **p < 0.01, ***p < 0.001 for protein interactions by Student's t test (C), for IPSC amplitudes analyzed by one-way ANOVA (Kruskal-Wallis test, H), for PPRs analyzed by two-way ANOVA (I); all comparisons with cDKO. For additional analyses of RIM C_2B-SNARE interactions and synaptotagmin-1 binding, see Figure S6. For assessment of rescue RIM expression, example traces of PPRs, and a rescue experiment in which the RIM C_2B domain was replaced by the extended synaptotagmin 2 C_2C domain, see Figures S7A–S7J.

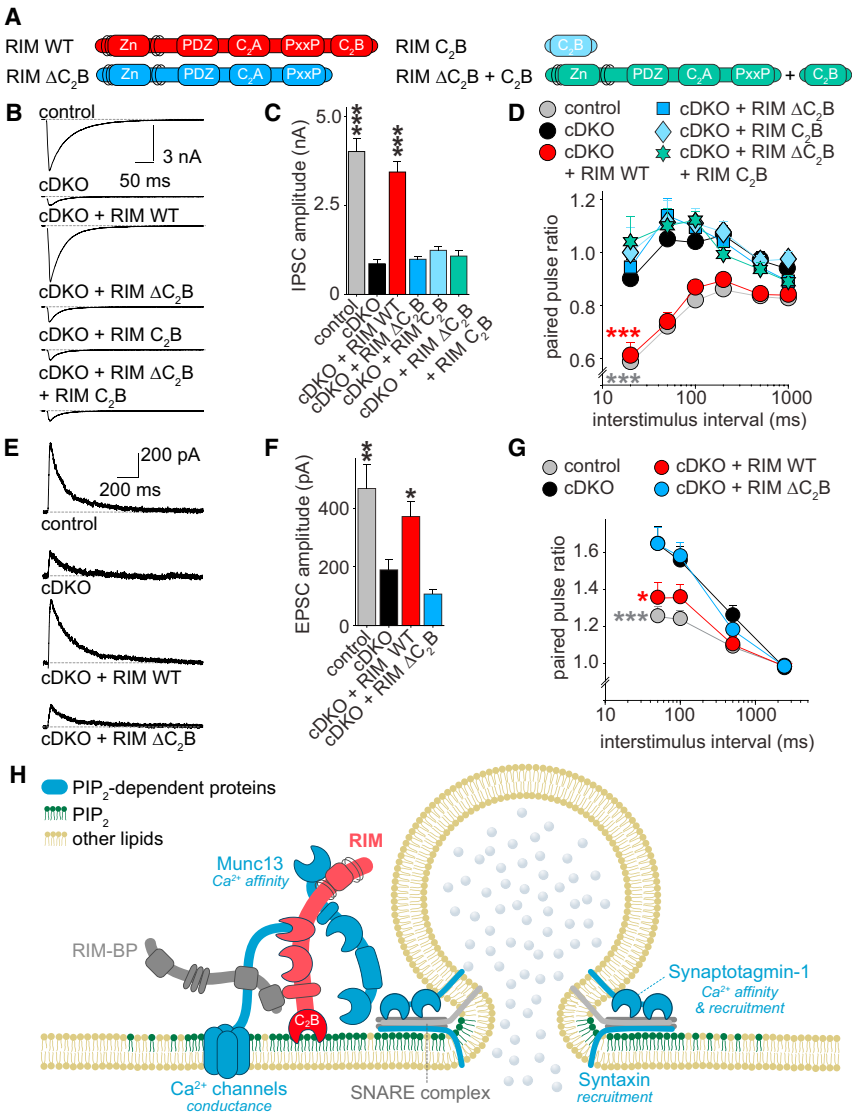

Figure 7. Tethering of RIM C_2B to N-Terminal RIM Domains Is Essential for Rescue

(A) Overview of rescue proteins.

(B and C) Example traces (B) and quantification of average amplitudes (C) of single evoked IPSCs. Control, n = 3 independent cultures/16 cells; cDKO, 3/15; cDKO + RIM WT, 3/16; cDKO + RIM ΔC_2B, 3/15; cDKO + RIM C_2B, 3/15; cDKO + RIM ΔC_2B + RIM C_2B, 3/15.

(D) Quantification of IPSC PPRs at various interstimulus intervals. The number of observations is as in (C).

(E and F) Example traces (E) and quantification of average amplitudes (F) of single evoked NMDA receptor EPSCs in cultured hippocampal neurons. Control, n = 4 independent cultures/18 cells; cDKO, 4/19; cDKO + RIM WT, 4/20; cDKO + RIM ΔC_2B, 4/19.

(G) Quantification of EPSC PPRs at various interstimulus intervals. The number of observations is as in (F).

(H) Working model for the roles of RIM C_2B at the active zone. C_2B targets RIM to PIP_2-containing membranes, recruiting its direct interaction partners and additional important fusion machinery to colocalize vesicle priming, Ca^{2+} influx, and fusion with PIP_2. Many proteins that are important for release are activated by PIP_2 (highlighted in blue, with the effect of PIP_2 indicated in italics). C_2B has an additional activity in synaptic vesicle release that may depend on PIP_2 at the active zone.

All data are shown as mean ± SEM; *p < 0.05, **p < 0.01, ***p < 0.001 for IPSC and EPSC amplitude analyzed by one-way ANOVA (Kruskal-Wallis test, C and F) and for PPRs analyzed by two-way ANOVA (D and G); all comparisons with cDKO. For analyses of rescue protein expression and example traces of PPRs, see Figures S7K–S7M.

The strong defect in PPR, contrasted by rescue of vesicle priming and Munc13 levels and localization (Figure 2), establishes a defect in *p*. RIM boosts Ca^{2+} influx (Han et al., 2011; Kaeser et al., 2011; Müller et al., 2012), which may explain a reduction in *p*. Previously, RIM C_2B was shown to inhibit voltage-dependent Ca^{2+} channel inactivation to enhance Ca^{2+} currents in transfected non-neuronal cells (Kaeser et al., 2012; Kiyonaka et al., 2007; Uriu et al., 2010), suggesting a direct role for C_2B in presynaptic Ca^{2+} influx. However, our experiments establish that RIM C_2B domains do not boost *p* through enhancing Ca^2 influx. First, we found that RIM ΔC_2B rescues Ca^{2+} influx (Figure 2). Second, train stimulation, which leads to high residual Ca^{2+} in nerve terminals, fails to boost vesicle fusion in RIM 4E-expressing neurons, indicating that the role of C_2B is downstream of Ca^{2+} influx (Figure S5). Third, RIM C_2B domains alone do not increase action potential-triggered release or its Ca^{2+} dependence in RIM cDKO neurons (Figure 7; Kaeser et al., 2011, 2012). Finally, the effect in heterologous cells was observed for all RIMs, including RIM3 (Uriu et al., 2010), but we found that substitution of RIM1 C_2B with RIM3 C_2B did not fully rescue *p* (Figure 6). Thus, RIM C_2B does not boost Ca^{2+} entry to enhance *p*. Importantly, RIM cDKO at the calyx of Held leads to reduced Ca^{2+} sensitivity of fusion when Ca^{2+} entry is bypassed with Ca^{2+} uncaging (Han et al., 2011), supporting that roles for RIM in *p* independent of Ca^{2+} entry exist. We conclude that C_2B mediates a new function of RIM independent of its activities in vesicle docking, priming, and Ca^{2+} entry.

Roles for RIM C_2B Binding to PIP_2 in Action Potential-Triggered Release

In rescue experiments using mutations in the polybasic sequence of C_2B, we identified a critical role for PIP_2 binding to the RIM C_2B domain for action potential-induced release (Figure 5). Could other interactions of the RIM C_2B domain contribute to the function of C_2B in vesicle fusion? As outlined above, it is unlikely that the previously identified interaction with β subunits of Ca^{2+} channels contributes via boosting Ca^{2+} influx. The RIM1 C_2B domain was also identified to bind to Liprin-α proteins (Schoch et al., 2002), and this interaction was

not affected by the C_2B 2E mutation (Figure 6). Remarkably, Liprin-α did not bind to RIM4 C_2B, but replacing RIM1 C_2B with the C_2B domain of RIM4 fully rescued fusion. Hence, binding of Liprin-α to RIM is either not important for neurotransmitter release, or functional redundancy with other RIM interactions masks important roles for Liprin-α RIM C_2B domain interactions.

Surprisingly, substitution with the RIM3 C_2B domain, which, like RIM4 C_2B, binds PIP_2 but not Liprin-α, led to incomplete rescue of synaptic transmission (Figure 6). In addition, exchanging C_2B with the C_2C domain of extended synaptotagmin-2, which, like C_2B, binds PIP_2 but not Ca^{2+} (Giordano et al., 2013), failed to rescue *p* or IPSC amplitudes (Figure S7). Thus, substituting C_2B with another PIP_2-binding C_2 domain is insufficient, indicating that RIM1 C_2B has additional roles in vesicle fusion that are also present in RIM4 C_2B. Interestingly, our data show that C_2B alone is insufficient to boost fusion in cDKO neurons (Figure 7; Kaeser et al., 2011, 2012) and that C_2B must be connected to the N-terminal RIM domains to rescue exocytosis (Figure 7). This indicates that its role at the active zone requires close proximity to the other RIM domains and their binding partners, and it is possible that C_2B engages in intramolecular interactions with other RIM domains.

Does RIM C_2B Localize Synaptic Vesicle Priming and Ca^{2+} Influx to PIP_2-Containing Membranes?

PIP_2 is required at the target membrane for efficient vesicle fusion (Hay et al., 1995; Milosevic et al., 2005; Di Paolo et al., 2004). Although the exact distribution of PIP_2 at the active zone is unknown, studies in non-neuronal cells showed that PIP_2 is clustered in small domains within the plasma membrane (van den Bogaart et al., 2011; Honigmann et al., 2013; Laux et al., 2000). Functions of many core components of the synaptic vesicle fusion machinery depend on interactions with PIP_2; for example, those of synaptotagmin, syntaxin, Munc13, and Ca^{2+} channels (Bai et al., 2004; van den Bogaart et al., 2011; Li et al., 2006; Shin et al., 2010; Suh et al., 2010). Multiple additional proteins that regulate synaptic vesicle exocytosis bind to PIP_2, including CAPS, Doc2, protein kinase C (PKC), and Rabphilin, and endocytosis is also dependent on PIP_2 (Koch and Holt, 2012; Lauwers et al., 2016). Hence, optimal fusion requires co-localization of PIP_2 with these proteins, and mis-targeting of the release machinery away from PIP_2-containing membranes would lead to impaired release with multiple proteins operating at sub-optimal capacity.

We propose that RIM C_2B domains target the release machinery to PIP_2-containing membranes (Figure 7H). This targeting mechanism could have several important implications for synaptic vesicle exocytosis. If PIP_2 is present at the active zone in small clusters, as has been observed in non-neuronal cells (Aoyagi et al., 2005; van den Bogaart et al., 2011; Honigmann et al., 2013), then this could provide for nanoscale scaffolding at PIP_2-rich fusion sites to integrate the functions of RIM, and potentially its PIP_2-dependent interaction partners, for efficient docking, priming, and Ca^{2+} triggering. Recent findings provide further support for this model. Within an active zone, synaptic vesicle exocytosis is restricted to a few sites (Maschi and Klyachko, 2017; Tang et al., 2016). These sites align in a nanocolumnar structure with postsynaptic receptor clusters and contain RIM as a central component. Remarkably, the diameter of these RIM clusters is ~80 nm (Tang et al., 2016), very similar to the diameter of syntaxin-associated PIP_2 clusters, which was determined to be 73 nm in non-neuronal secretory cells (van den Bogaart et al., 2011). The exact distribution of PIP_2 within an active zone and the underlying clustering mechanisms are currently unknown because the available tools have not allowed measuring PIP_2 clustering at synapses. In the model in which RIM targets release to PIP_2-containing fusion sites, we favor that PIP_2 clusters RIM and its activities in exocytosis because there are likely many more PIP_2 molecules than RIM molecules in a nerve terminal. However, it is possible that RIM has an active role in generating PIP_2 clusters or that PIP_2 activates other RIM activities. Ultimately, the functional effects of these alternative possibilities are similar: they all lead to fusion sites where essential activities of RIM and PIP_2 are tethered to one another for efficient exocytosis.

Because the extent of nanoscale clustering of PIP_2 at the active zone is not well known, other potential roles of PIP_2-RIM interactions need to be considered. It is well established that PIP_2 defines the plasma membrane identity (Di Paolo and De Camilli, 2006) independent of how it is clustered. Hence, it is possible that the targeting function of RIM-PIP_2 interactions is necessary to assemble the fusion machinery in the correct orientation for efficient release or that this interaction provides a proofreading mechanism to ensure that exocytosis occurs at the correct target membrane. The apparent specificity of C_2B for the $PI(4,5)P_2$ isomer (Figure S4) would be in line with the latter model because this isomer is almost exclusively present in the plasma membrane (Di Paolo and De Camilli, 2006). Finally, because RIM C_2B has additional roles in fusion (Figures 6 and S7), it is possible that these roles are activated by PIP_2. In a similar fashion, Ca^{2+} binding to synaptotagmin-1 C_2B is likely activated by PIP_2 (Bai et al., 2004; van den Bogaart et al., 2012).

We have identified an unexpected, important role for RIM C_2B in the control of synaptic vesicle exocytosis. Our data suggest that the function of RIM at the active zone reaches beyond docking, priming, and tethering of Ca^{2+} channels but directly regulates the efficiency of fusion by interacting with essential membrane lipids. RIM and PIP_2 have important roles in fusion outside of the nervous system (Hay et al., 1995; Milosevic et al., 2005; Yasuda et al., 2010), and many additional C_2 domain proteins are Ca^{2+} independent but have polybasic sequences in their C_2 domains similar to RIM. Hence, the constitutive tethering of C_2 domain scaffolds to PIP_2-rich membranes may provide for a mechanism across diverse secretory pathways to target exocytosis to specific membrane domains.

STAR★METHODS

Detailed methods are provided in the online version of this paper and include the following:

- KEY RESOURCES TABLE
- CONTACT FOR REAGENT AND RESOURCE SHARING
- EXPERIMENTAL MODELS AND SUBJECT DETAILS
  - Mice

SUPPLEMENTAL INFORMATION

Supplemental Information includes seven figures and can be found with this article online at https://doi.org/10.1016/j.neuron.2018.03.011.

ACKNOWLEDGMENTS

We thank Lydia Bickford and Jennifer Jiexin Wang for technical support, Hajnalka Nyitrai for help with antibody production, Dr. Thomas Südhof for antibodies, and Dr. Jonathan Cohen and members of the Kaeser laboratory for comments on the manuscript. This work was supported by grants from the NIH (R01NS083898 and R01MH113349 to P.S.K. and R35NS097333 to J.R.), the Lefler Foundation (to A.d.J.), the NWO (Rubicon Fellowship 825.12.028 to A.d.J.), the Harvard Brain Initiative (to P.S.K.), and the Welch Foundation (I-1304 to J.R.). The Agilent DD2 consoles of the 800 MHz spectrometer and one of the 600 MHz spectrometers used for the research presented here were purchased with shared instrumentation grants from the NIH (S10OD018027 to J.R. and S10RR026461 to Michael K. Rosen). We also acknowledge the Neurobiology Imaging Facility (supported by the Core Center grant P30NS072030) and the Harvard Neurodiscovery Imaging Center.

AUTHOR CONTRIBUTIONS

Conceptualization, A.P.H.d.J., J.R., and P.S.K.; Methodology, A.P.H.d.J., J.R., and P.S.K.; Formal Analysis, A.P.H.d.J., M.-R.H., C.M.R., J.R., and P.S.K.; Investigation, A.P.H.d.J., M.-R.H., C.M.R., M.Y.W., and C.A.B.; Writing-Original Draft, A.P.H.d.J. and P.S.K.; Supervision, J.R. and P.S.K.; Funding Acquisition A.P.H.d.J., J.R., and P.S.K.

DECLARATION OF INTERESTS

The authors declare no competing interests.

Received: September 28, 2017
Revised: February 1, 2018
Accepted: March 5, 2018
Published: March 29, 2018

REFERENCES

Andrews-Zwilling, Y.S., Kawabe, H., Reim, K., Varoqueaux, F., and Brose, N. (2006). Binding to Rab3A-interacting molecule RIM regulates the presynaptic recruitment of Munc13-1 and ubMunc13-2. J. Biol. Chem. *281*, 19720–19731.

Aoyagi, K., Sugaya, T., Umeda, M., Yamamoto, S., Terakawa, S., and Takahashi, M. (2005). The activation of exocytotic sites by the formation of phosphatidylinositol 4,5-bisphosphate microdomains at syntaxin clusters. J. Biol. Chem. *280*, 17346–17352.

Augustin, I., Rosenmund, C., Südhof, T.C., and Brose, N. (1999). Munc13-1 is essential for fusion competence of glutamatergic synaptic vesicles. Nature *400*, 457–461.

Bai, J., Tucker, W.C., and Chapman, E.R. (2004). PIP2 increases the speed of response of synaptotagmin and steers its membrane-penetration activity toward the plasma membrane. Nat. Struct. Mol. Biol. *11*, 36–44.

van den Bogaart, G., Meyenberg, K., Risselada, H.J., Amin, H., Willig, K.I., Hubrich, B.E., Dier, M., Hell, S.W., Grubmüller, H., Diederichsen, U., and Jahn, R. (2011). Membrane protein sequestering by ionic protein-lipid interactions. Nature *479*, 552–555.

van den Bogaart, G., Meyenberg, K., Diederichsen, U., and Jahn, R. (2012). Phosphatidylinositol 4,5-bisphosphate increases Ca2+ affinity of synaptotagmin-1 by 40-fold. J. Biol. Chem. *287*, 16447–16453.

Brautigam, C.A. (2015). Calculations and Publication-Quality Illustrations for Analytical Ultracentrifugation Data. Methods Enzymol. *562*, 109–133.

Camacho, M., Basu, J., Trimbuch, T., Chang, S., Pulido-Lozano, C., Chang, S.-S., Duluvova, I., Abo-Rady, M., Rizo, J., and Rosenmund, C. (2017). Heterodimerization of Munc13 C_2A domain with RIM regulates synaptic vesicle docking and priming. Nat. Commun. *8*, 15293.

Coppola, T., Magnin-Lüthi, S., Perret-Menoud, V., Gattesco, S., Schiavo, G., and Regazzi, R. (2001). Direct interaction of the Rab3 effector RIM with Ca2+ channels, SNAP-25, and synaptotagmin. J. Biol. Chem. *276*, 32756–32762.

Corbalan-Garcia, S., and Gómez-Fernández, J.C. (2014). Signaling through C2 domains: more than one lipid target. Biochim. Biophys. Acta *1838*, 1536–1547.

Coudevylle, N., Montaville, P., Leonov, A., Zweckstetter, M., and Becker, S. (2008). Structural determinants for Ca2+ and phosphatidylinositol 4,5-bisphosphate binding by the C2A domain of rabphilin-3A. J. Biol. Chem. *283*, 35918–35928.

Dai, H., Tomchick, D.R., García, J., Südhof, T.C., Machius, M., and Rizo, J. (2005). Crystal structure of the RIM2 C2A-domain at 1.4 A resolution. Biochemistry *44*, 13533–13542.

Delaglio, F., Grzesiek, S., Vuister, G.W., Zhu, G., Pfeifer, J., and Bax, A. (1995). NMRPipe: a multidimensional spectral processing system based on UNIX pipes. J. Biomol. NMR *6*, 277–293.

Deng, L., Kaeser, P.S., Xu, W., and Südhof, T.C. (2011). RIM proteins activate vesicle priming by reversing autoinhibitory homodimerization of Munc13. Neuron *69*, 317–331.

Eggermann, E., Bucurenciu, I., Goswami, S.P., and Jonas, P. (2011). Nanodomain coupling between Ca^{2+} channels and sensors of exocytosis at fast mammalian synapses. Nat. Rev. Neurosci. *13*, 7–21.

Giordano, F., Saheki, Y., Idevall-Hagren, O., Colombo, S.F., Pirruccello, M., Milosevic, I., Gracheva, E.O., Bagriantsev, S.N., Borgese, N., and De Camilli, P. (2013). PI(4,5)P(2)-dependent and Ca(2+)-regulated ER-PM interactions mediated by the extended synaptotagmins. Cell *153*, 1494–1509.

Groffen, A.J., Martens, S., Díez Arazola, R., Cornelisse, L.N., Lozovaya, N., de Jong, A.P.H., Goriounova, N.A., Habets, R.L.P., Takai, Y., Borst, J.G., et al. (2010). Doc2b is a high-affinity Ca2+ sensor for spontaneous neurotransmitter release. Science *327*, 1614–1618.

Guan, R., Dai, H., Tomchick, D.R., Dulubova, I., Machius, M., Südhof, T.C., and Rizo, J. (2007). Crystal structure of the RIM1alpha C2B domain at 1.7 A resolution. Biochemistry *46*, 8988–8998.

Guan, R., Dai, H., and Rizo, J. (2008). Binding of the Munc13-1 MUN domain to membrane-anchored SNARE complexes. Biochemistry *47*, 1474–1481.

Guerrero-Valero, M., Ferrer-Orta, C., Querol-Audí, J., Marin-Vicente, C., Fita, I., Gómez-Fernández, J.C., Verdaguer, N., and Corbalán-García, S. (2009). Structural and mechanistic insights into the association of PKCalpha-C2 domain to PtdIns(4,5)P2. Proc. Natl. Acad. Sci. USA *106*, 6603–6607.

Han, Y., Kaeser, P.S., Südhof, T.C., and Schneggenburger, R. (2011). RIM determines Ca^{2}+ channel density and vesicle docking at the presynaptic active zone. Neuron *69*, 304–316.

Hay, J.C., Fisette, P.L., Jenkins, G.H., Fukami, K., Takenawa, T., Anderson, R.A., and Martin, T.F. (1995). ATP-dependent inositide phosphorylation required for Ca(2+)-activated secretion. Nature *374*, 173–177.

Hibino, H., Pironkova, R., Onwumere, O., Vologodskaia, M., Hudspeth, A.J., and Lesage, F. (2002). RIM binding proteins (RBPs) couple Rab3-interacting molecules (RIMs) to voltage-gated Ca(2+) channels. Neuron *34*, 411–423.

Honigmann, A., van den Bogaart, G., Iraheta, E., Risselada, H.J., Milovanovic, D., Mueller, V., Müllar, S., Diederichsen, U., Fasshauer, D., Grubmüller, H., et al. (2013). Phosphatidylinositol 4,5-bisphosphate clusters act as molecular beacons for vesicle recruitment. Nat. Struct. Mol. Biol. *20*, 679–686.

Imig, C., Min, S.W., Krinner, S., Arancillo, M., Rosenmund, C., Südhof, T.C., Rhee, J., Brose, N., and Cooper, B.H. (2014). The morphological and molecular nature of synaptic vesicle priming at presynaptic active zones. Neuron *84*, 416–431.

Jahn, R., and Fasshauer, D. (2012). Molecular machines governing exocytosis of synaptic vesicles. Nature *490*, 201–207.

Johnson, B.A., and Blevins, R.A. (1994). NMR View: A computer program for the visualization and analysis of NMR data. J. Biomol. NMR *4*, 603–614.

Johnson, S., Halford, S., Morris, A.G., Patel, R.J., Wilkie, S.E., Hardcastle, A.J., Moore, A.T., Zhang, K., and Hunt, D.M. (2003). Genomic organisation and alternative splicing of human RIM1, a gene implicated in autosomal dominant cone-rod dystrophy (CORD7). Genomics *81*, 304–314.

Kaeser, P.S., and Regehr, W.G. (2017). The readily releasable pool of synaptic vesicles. Curr. Opin. Neurobiol. *43*, 63–70.

Kaeser, P.S., Kwon, H.-B., Chiu, C.Q., Deng, L., Castillo, P.E., and Südhof, T.C. (2008). RIM1alpha and RIM1beta are synthesized from distinct promoters of the RIM1 gene to mediate differential but overlapping synaptic functions. J. Neurosci. *28*, 13435–13447.

Kaeser, P.S., Deng, L., Wang, Y., Dulubova, I., Liu, X., Rizo, J., and Südhof, T.C. (2011). RIM proteins tether Ca2+ channels to presynaptic active zones via a direct PDZ-domain interaction. Cell *144*, 282–295.

Kaeser, P.S., Deng, L., Fan, M., and Südhof, T.C. (2012). RIM genes differentially contribute to organizing presynaptic release sites. Proc. Natl. Acad. Sci. USA *109*, 11830–11835.

Kiyonaka, S., Wakamori, M., Miki, T., Uriu, Y., Nonaka, M., Bito, H., Beedle, A.M., Mori, E., Hara, Y., De Waard, M., et al. (2007). RIM1 confers sustained activity and neurotransmitter vesicle anchoring to presynaptic Ca2+ channels. Nat. Neurosci. *10*, 691–701.

Koch, M., and Holt, M. (2012). Coupling exo- and endocytosis: An essential role for PIP2 at the synapse. Biochim. Biophys. Acta - Mol. Cell Biol. Lipids *1821*, 1114–1132.

Koushika, S.P., Richmond, J.E., Hadwiger, G., Weimer, R.M., Jorgensen, E.M., and Nonet, M.L. (2001). A post-docking role for active zone protein Rim. Nat. Neurosci. *4*, 997–1005.

Lauwers, E., Goodchild, R., and Verstreken, P. (2016). Membrane Lipids in Presynaptic Function and Disease. Neuron *90*, 11–25.

Laux, T., Fukami, K., Thelen, M., Golub, T., Frey, D., and Caroni, P. (2000). GAP43, MARCKS, and CAP23 modulate PI(4,5)P(2) at plasmalemmal rafts, and regulate cell cortex actin dynamics through a common mechanism. J. Cell Biol. *149*, 1455–1472.

Li, L., Shin, O.H., Rhee, J.S., Araç, D., Rah, J.C., Rizo, J., Südhof, T., and Rosenmund, C. (2006). Phosphatidylinositol phosphates as co-activators of Ca2+ binding to C2 domains of synaptotagmin 1. J. Biol. Chem. *281*, 15845–15852.

Liu, K.S., Siebert, M., Mertel, S., Knoche, E., Wegener, S., Wichmann, C., Matkovic, T., Muhammad, K., Depner, H., Mettke, C., et al. (2011). RIM-binding protein, a central part of the active zone, is essential for neurotransmitter release. Science *334*, 1565–1569.

Maschi, D., and Klyachko, V.A. (2017). Spatiotemporal Regulation of Synaptic Vesicle Fusion Sites in Central Synapses. Neuron *94*, 65–73.e3.

Maximov, A., Pang, Z.P., Tervo, D.G.R., and Südhof, T.C. (2007). Monitoring synaptic transmission in primary neuronal cultures using local extracellular stimulation. J. Neurosci. Methods *161*, 75–87.

Milosevic, I., Sørensen, J.B., Lang, T., Krauss, M., Nagy, G., Haucke, V., Jahn, R., and Neher, E. (2005). Plasmalemmal phosphatidylinositol-4,5-bisphosphate level regulates the releasable vesicle pool size in chromaffin cells. J. Neurosci. *25*, 2557–2565.

Montaville, P., Coudevylle, N., Radhakrishnan, A., Leonov, A., Zweckstetter, M., and Becker, S. (2008). The PIP2 binding mode of the C2 domains of rabphilin-3A. Protein Sci. *17*, 1025–1034.

Müller, M., Liu, K.S.Y., Sigrist, S.J., and Davis, G.W. (2012). RIM controls homeostatic plasticity through modulation of the readily-releasable vesicle pool. J. Neurosci. *32*, 16574–16585.

Di Paolo, G., and De Camilli, P. (2006). Phosphoinositides in cell regulation and membrane dynamics. Nature *443*, 651–657.

Di Paolo, G., Moskowitz, H.S., Gipson, K., Wenk, M.R., Voronov, S., Obayashi, M., Flavell, R., Fitzsimonds, R.M., Ryan, T.A., and De Camilli, P. (2004). Impaired PtdIns(4,5)P2 synthesis in nerve terminals produces defects in synaptic vesicle trafficking. Nature *431*, 415–422.

Rosenmund, C., and Stevens, C.F. (1996). Definition of the readily releasable pool of vesicles at hippocampal synapses. Neuron *16*, 1197–1207.

Schoch, S., Castillo, P.E., Jo, T., Mukherjee, K., Geppert, M., Wang, Y., Schmitz, F., Malenka, R.C., and Südhof, T.C. (2002). RIM1α forms a protein scaffold for regulating neurotransmitter release at the active zone. Nature *415*, 321–326.

Schuck, P. (2000). Size-distribution analysis of macromolecules by sedimentation velocity ultracentrifugation and lamm equation modeling. Biophys. J. *78*, 1606–1619.

Schuck, P. (2003). On the analysis of protein self-association by sedimentation velocity analytical ultracentrifugation. Anal. Biochem. *320*, 104–124.

Shin, O.-H., Lu, J., Rhee, J.-S., Tomchick, D.R., Pang, Z.P., Wojcik, S.M., Camacho-Perez, M., Brose, N., Machius, M., Rizo, J., et al. (2010). Munc13 C2B domain is an activity-dependent Ca2+ regulator of synaptic exocytosis. Nat. Struct. Mol. Biol. *17*, 280–288.

Südhof, T.C. (2012). The presynaptic active zone. Neuron *75*, 11–25.

Südhof, T.C. (2013). Neurotransmitter release: the last millisecond in the life of a synaptic vesicle. Neuron *80*, 675–690.

Suh, B.C., Leal, K., and Hille, B. (2010). Modulation of high-voltage activated Ca(2+) channels by membrane phosphatidylinositol 4,5-bisphosphate. Neuron *67*, 224–238.

Tang, A.-H., Chen, H., Li, T.P., Metzbower, S.R., MacGillavry, H.D., and Blanpied, T.A. (2016). A trans-synaptic nanocolumn aligns neurotransmitter release to receptors. Nature *536*, 210–214.

Ubach, J., Lao, Y., Fernandez, I., Arac, D., Südhof, T.C., and Rizo, J. (2001). The C2B domain of synaptotagmin I is a Ca2+-binding module. Biochemistry *40*, 5854–5860.

Uriu, Y., Kiyonaka, S., Miki, T., Yagi, M., Akiyama, S., Mori, E., Nakao, A., Beedle, A.M., Campbell, K.P., Wakamori, M., and Mori, Y. (2010). Rab3-interacting molecule γ isoforms lacking the Rab3-binding domain induce long lasting currents but block neurotransmitter vesicle anchoring in voltage-dependent P/Q-type Ca2+ channels. J. Biol. Chem. *285*, 21750–21767.

Wang, Y., and Südhof, T.C. (2003). Genomic definition of RIM proteins: evolutionary amplification of a family of synaptic regulatory proteins. Genomics *81*, 126–137.

Wang, S.S.H., Held, R.G., Wong, M.Y., Liu, C., Karakhanyan, A., and Kaeser, P.S. (2016). Fusion Competent Synaptic Vesicles Persist upon Active Zone Disruption and Loss of Vesicle Docking. Neuron *91*, 777–791.

Wickner, W. (2010). Membrane fusion: five lipids, four SNAREs, three chaperones, two nucleotides, and a Rab, all dancing in a ring on yeast vacuoles. Annu. Rev. Cell Dev. Biol. *26*, 115–136.

Wong, M.Y., Liu, C., Wang, S.S.H., Roquas, A.C.F., Fowler, S., and Kaeser, P.S. (2018). Liprin-α3 controls vesicle docking and exocytosis at the active

zone of hippocampal synapses. Proc. Natl. Acad. Sci. USA *115*, 2234–2239.

Yasuda, T., Shibasaki, T., Minami, K., Takahashi, H., Mizoguchi, A., Uriu, Y., Numata, T., Mori, Y., Miyazaki, J., Miki, T., and Seino, S. (2010). Rim2alpha determines docking and priming states in insulin granule exocytosis. Cell Metab. *12*, 117–129.

Zhao, H., Brautigam, C.A., Ghirlando, R., and Schuck, P. (2013). Overview of current methods in sedimentation velocity and sedimentation equilibrium analytical ultracentrifugation. Curr. Protoc. Protein Sci. *Chapter 20*, 12.

Zucker, R.S., and Regehr, W.G. (2002). Short-term synaptic plasticity. Annu. Rev. Physiol. *64*, 355–405.

STAR★METHODS

KEY RESOURCES TABLE

REAGENT or RESOURCE	SOURCE	IDENTIFIER
Antibodies		
Rabbit polyclonal anti-RIM central domains (R809)	Schoch et al., 2002	RRID:AB_2617051
Rabbit polyclonal anti-RIM C-terminal (U1130)	Schoch et al., 2002	n/a
Rabbit polyclonal anti-RIM central domains (HM1092)	This study	n/a
Rabbit polyclonal anti-liprin-α LH2 domain (4396)	Schoch et al., 2002	RRID:AB_2617056
Rabbit polyclonal anti-synaptotagmin cytoplasmic domain (V216)	Südhof laboratory	n/a
Mouse monoclonal anti-CaV β2 (clone N10/7)	NeuroMab	Cat # 73-054
		RRID:AB_10671176
Rabbit polyclonal anti-SNAP-25 (P913)	Südhof Laboratory	n/a
Rabbit polyclonal anti-Synaptobrevin-2 (P939)	Südhof Laboratory	n/a
Rabbit polyclonal anti-Syntaxin-1 (438B)	Südhof Laboratory	n/a
Mouse monoclonal anti-HA (clone 16B12)	Covance	Cat # MMS-101P
		RRID: AB_2314672
Mouse monoclonal anti-β-actin (clone AC-15)	Sigma	Cat # A1978
		RRID:AB_476692
Rabbit polyclonal anti-Munc13-1 C_2A domain	SySy	Cat # 126 111
		RRID:AB_887735
Rabbit polyclonal anti-RIM PDZ domain	SySy	Cat # 140 003
		RRID:AB_887774
Rabbit polyclonal anti-RIM PDZ domain	BD Bioscience	Cat# 610907
		RRID:AB_10611855
Guinea pig polyclonal anti-Synaptophysin	SySy	Cat# 101 004
		RRID:AB_1210382
Mouse monoclonal anti-Bassoon (clone SAP7F407)	Enzo life sciences	Cat# ADI-VAM-PS003
		RRID:AB_11181058
Guinea pig polyclonal anti-vGAT cytoplasmic domain	SySy	Cat #131 004
		RRID: AB_887873
Chemicals, Peptides, and Recombinant Proteins		
L-α-phosphatidylinositol-4,5-bisphosphate	Avanti	Cat #840046X
L-α-phosphatidylcholine	Avanti	Cat #840032C
L-α-phosphatidylserine	Avanti	Cat #840032C
1,2-dioleoyl-sn-glycero-3-phospho-(1'-myo-inositol-3′, 4'-bisphosphate)	Avanti	Cat #850153P
1,2-dioleoyl-sn-glycero-3-phospho-(1'-myo-inositol-3′, 5′-bisphosphate)	Avanti	Cat #850154P
1,2-dioleoyl-sn-glycero-3-phospho-(1'-myo-inositol-3′, 4',5′-trisphosphate)	Avanti	Cat #850156P
1,2-dioleoyl-sn-glycero-3-[phospho-L-serine]	Avanti	Cat # 840035
1-palmitoyl-2-oleoyl-sn-glycero-3-phosphocholine	Avanti	Cat # 850457
1,2-dipalmitoyl-sn-glycero-3-phosphoethanolamine-N-(lissamine rhodamine B sulfonyl)	Avanti	Cat # 810158C
L-α-Phosphatidylinositol-4-phosphate	Avanti	Cat # 840045X
L-α-Phosphatidylinositol	Avanti	Cat # 840042C
dibutanoyl phosphatidylinositol 4,5-bisphosphate (diC4-PIP_2)	Echelon	Cat # P4504

(*Continued on next page*)

Continued

REAGENT or RESOURCE	SOURCE	IDENTIFIER
CNQX	Tocris	Cat #0190
D-APV	Tocris	Cat #0106
Picrotoxin	Tocris	Cat #1128
QX-314	Tocris	Cat #2313
Tedrodotoxin	Tocris	Cat #1078
Fluo5F pentapotassium salt	Thermo Fisher	Cat #F-14221
Alexa 647 hydrazide	Thermo Fisher	Cat #A-20502
Fugene HD	Promega	Cat #E2312
Experimental Models: Cell Lines		
HEK293T/17 cells	ATCC	RRID: CVCL_0063
Experimental Models: Organisms/Strains		
Mouse *Rims1*^{tm3Sud}/J	Kaeser et al., 2008	RRID:IMSR_JAX:015832
Mouse *Rims2*$^{tm1.1Sud}$/J	Kaeser et al., 2011	RRID:IMSR_JAX:015833
Recombinant DNA		
pAJ14063 pFUGW RIM1a WT HA	This study	n/a
pAJ14064 pFUGW RIM1a B2E HA	This study	n/a
pAJ14065 pFUGW RIM1a 4E HA	This study	n/a
pAJ14066 pFUGW RIM1a A2E HA	This study	n/a
pAJ15020 pFUGW RIM1a HA ΔC2B	This study	n/a
pAJ15019 pFUGW RIM1-3 HA	This study	n/a
pAJ15032 pFUGW RIM1-4 HA	This study	n/a
pAJ13005 pGEX RIM1a C2B WT	This study	n/a
pAJ13014 pGEX RIM1a C2B 2E	This study	n/a
pAJ13023 pET RIM1a C2B WT	This study	n/a
pAJ13026 pGEX RIM1a C2A WT	This study	n/a
pAJ13027 pGEX RIM2a C2A WT	This study	n/a
pAJ13028 pGEX RIM2a C2B WT	This study	n/a
pAJ14006 pET RIM1a C2B 2E	This study	n/a
pAJ14016 pGEX RIM1 C2A 2E	This study	n/a
pAJ14021 pET RIM1 C2A WT	This study	n/a
pAJ14022 pET RIM1 C2A 834,835E	This study	n/a
pAJ14046 pET RIM3 C2B WT	This study	n/a
pAJ14047 pET RIM4 C2B WT	This study	n/a
pAJ15025 pGEX RIM3 C2B WT	This study	n/a
pAJ15026 pGEX RIM4 C2B WT	This study	n/a
pAJ16001 pET RIM1 C2B K1513E	This study	n/a
pAJ16002 pET RIM1 C2B K1515E	This study	n/a
pAJ16003 pET RIM1 C2B Y1499S	This study	n/a
pAJ16004 pET RIM1 C2B Y1499S,K1501E	This study	n/a
pAJ16005 pET RIM1 C2B K1513,K1515A	This study	n/a
pAJ16006 pET RIM1 C2B K1501E	This study	n/a
pAJ16008 pET RIM1 C2B K1556E	This study	n/a
pAJ16009 RIM1 PDZ(491-772)	This study	n/a
pAJ17013 pFUGW RIM1a ΔC2A HA	This study	n/a
pAJ17015 pFUGW Cre 2A myc RIM1 C2B WT	This study	n/a
pAJ17016 pFUGW RIM1a ΔC2B – C2C(Esyt2)	This study	n/a
pMYW12035 pGEX Liprin-α3-LH1	This study	n/a
pMYW12036 pGEX Liprin-α3-LH2	This study	n/a

(*Continued on next page*)

Continued

REAGENT or RESOURCE	SOURCE	IDENTIFIER
pFSW-Cre	Wang et al., 2016	n/a
pFSW-ΔCre	Wang et al., 2016	n/a
pFUGW-Cre	Kaeser et al., 2011	n/a
pFUGW-ΔCre	Kaeser et al., 2011	n/a
pGEX-KT Rim1 C2B WT	Guan et al., 2007	
pGEX-KT Rim1 C2B K1513,K1515E	This study	n/a
pGEX-KT Rim1 C2A WT	This study	n/a
pGEX-KT Rim1 C2A WT R834, R835E	This study	
pGEX-KT Rim1 C2A WT K809,R811E	This study	
pET28A SNAP-25	Südhof laboratory	
pGEX-KT Syntaxin1	Südhof laboratory	
Software and Algorithms		
MATLAB 2016b	The Mathworks	RRID:SCR_001622
pClamp 10	Axon Instruments	https://www.moleculardevices.com/systems/axon-conventional-patch-clamp
ImageJ	NIH	RRID:SCR_003070
DNAStar 14	DNAStar	https://www.dnastar.com/
NMRPipe	IBBR	https://www.ibbr.umd.edu/nmrpipe/install.html
NMRView	One Moon Scientific	http://www.onemoonscientific.com/nmrviewj
SEDFIT	Schuck, 2000	http://www.analyticalultracentrifugation.com/default.htm
SEDPHAT	Schuck, 2003	http://www.analyticalultracentrifugation.com/sedphat/default.htm
GUSSI	Brautigam, 2015	RRID:SCR_011724 http://biophysics.swmed.edu/MBR/software.html

CONTACT FOR REAGENT AND RESOURCE SHARING

Requests for reagents and resource sharing should be directed to the Lead Contact, Pascal S. Kaeser, at kaeser@hms.harvard.edu.

EXPERIMENTAL MODELS AND SUBJECT DETAILS

Mice

RIM1/2 conditional knockout mice were previously described (Kaeser et al., 2011) and were maintained as homozygote lines in which the *Rims1* gene (RRID:IMSR_JAX:015832 (Kaeser et al., 2008)) and the *Rims2* gene (RRID:IMSR_JAX:015833 (Kaeser et al., 2011)) contained essential exons flanked by *loxp* sites. All animal experiments were approved by the Harvard University Animal Care and Use Committee.

Neuronal cell cultures and lentiviral infection

Dissociated high-density hippocampal cultures were prepared from newborn RIM1/2 conditional double knockout mice of either sex as described (Kaeser et al., 2008; Maximov et al., 2007). Lentiviruses were produced in HEK293T cells. HEK cells were maintained in DMEM supplemented with 10% bovine serum and 1% penicillin/streptomycin and were split every 2 days to maintain optimal growth rate. For virus production, HEK cells in neuronal culture media were transfected using Fugene (Promega) with 3rd generation lentiviral packaging plasmids (REV, RRE and VSV-G) and a separate lentiviral plasmid (FSW or FUGW) encoding the recombinant gene of interest. After 48 h, the culture medium was harvested and centrifuged for 5 min at 700 x *g*, and the supernatant was used immediately for infection. Neuronal cultures were infected at 4 days *in vitro* (DIV) with lentiviruses expressing GFP-Cre with enhanced nuclear localization driven by a ubiquitin (for electrophysiology) or synapsin promoter (for Ca^{2+}-imaging) to generate cDKO neurons or an inactivate, truncated variant of GFP-Cre to generate control neurons (Kaeser et al., 2011). For rescue expression of full-length RIM1α or mutant RIM, cultures were infected with a separate rescue virus containing a ubiquitin-promotor driven RIM open reading frame with an HA tag immediately following the PxxP motif (plasmid pAJ14063 for full-length RIM1α, (Kaeser et al., 2011)).

METHOD DETAILS

Lentiviral rescue constructs

To obtain a RIM ΔC_2B construct, full length RIM1α was truncated at the residue immediately preceding C_2B, following the definition of (Guan et al., 2007), the last residues being …FLDGL-stop (pAJ15020). In all constructs where C_2B is substituted with another domain, the substituting domain was fused directly to RIM ΔC_2B without additional linker sequences. RIM3 C_2B (residues GPAQI…SPSCS, pAJ15019) and RIM4-C_2B (residues GPAQF…CGERS, pAJ15032) were obtained from rat, Extended Synaptotagmin-2 C_2C (residues RLRQL…PQAMT, Addgene #66831, (Giordano et al., 2013), pAJ17016) from human. For co-expression of RIM ΔC_2B and C_2B in Figure 7, RIM1 C_2B (residues GPAQL…PCIRS-stop) was fused to Cre with a 2A sequence (pAJ17015). Successful expression of both open reading frames was confirmed by western blotting. To obtain RIM1 ΔC_2A, the sequence between residues DAPQV…HDESS in RIM1α was substituted with a short linker sequence (GSGA, pAJ17013)). Point mutations in C_2A and C_2B were generated by site-directed mutagenesis (pAJ14064, pAJ14065, pAJ14066). Expression of rescue constructs was confirmed by western blotting for every culture.

Electrophysiology

Whole-cell patch-clamp recordings were performed in cultured hippocampal neurons at DIV14-17 as described in (Maximov et al., 2007; Wang et al., 2016) at room temperature. Extracellular solution contained (in mM) 140 NaCl, 5 KCl, 2 $CaCl_2$, 2 $MgCl_2$, 10 HEPES (pH 7.4) and 10 Glucose. Borosilicate glass pipettes (2.5 - 4.5 MΩ) were filled with intracellular solution containing (in mM) 40 CsCl, 90 K-gluconate, 1.8 NaCl, 1.7 $MgCl_2$, 3.5 KCl, 0.05 EGTA, 10 HEPES (pH 7.4), 2 ATP-Mg, 0.4 GTP-Na_2, 10 phosphocreatine, 4 QX314-Cl. Cells were clamped at -70 mV, with $R_{series} < 15$ MΩ, and R_{series} was compensated online until $R_{access} = 0.6 – 1.1$ MΩ (typically 50%–70%). Action potential-evoked IPSCs were elicited by local electric stimulation and recorded in extracellular solution supplemented with 20 μM 6-cyano-7-nitroquinoxaline-2,3-dione (CNQX) and 50 μM (2R)-amino-5-phosphonovaleric acid (D-AP5). Evoked EPSCs were recorded in extracellular solution supplemented with 20 μM CNQX and 20 μM picrotoxin (PTX), and cells were clamped at +40 mV. For RRP measurements, 500 mM hypertonic sucrose was applied for 10 s by local perfusion (Rosenmund and Stevens, 1996), in the presence of 20 μM CNQX, 50 μM D-AP5 and 1 μM tedrodotoxin (TTX). The integral of the first 10 s of the response was used as measure of the RRP. Data were acquired using a Multiclamp 700B amplifier and a Digidata 1550 digitizer, recorded at 10 kHz, and filtered at 2 kHz. Data were analyzed using pClamp and custom written programs in MATLAB. For all electrophysiological experiments and analyses, the experimenter was blind to the experimental condition.

Ca^{2+} imaging

Imaging of presynaptic Ca^{2+}-transients was performed as described in (Wang et al., 2016) with minor modifications. Neurons were recorded at DIV14-16 with whole-cell patch clamp electrophysiology at room temperature in extracellular solution supplemented with 20 μM CNQX, 50 μM D-AP5 and 20 μM PTX. Intracellular solution contained (in mM) 140 K-Gluconate, 0.1 EGTA, 2 $MgCl_2$, 4 Na_2ATP, 1 NaGTP, 0.3 Fluo5-F, 0.03 AlexaFluor-647, 10 HEPES (pH 7.4). Because of the limited time window during which this experiment needs to be done and its laborious nature, we could only analyze three conditions at a time, and hence we compared RIM cDKO neurons to cDKO neurons rescued with RIM WT or RIM ΔC_2B. After filling for 7 minutes in current clamp ($V_m < -50$ mV at I = 0 pA), boutons were identified in the Alexa channel, based on their typical bead-like morphology. After 10 minutes of filling, cells were held at $V_m = -60$ mV, and action potentials were triggered using a somatic current injection (5 ms, 800-1500 pA). Fluo5-F was excited with a pE-4000 LED at 470 nm (CoolLED) at 75% intensity. Images were acquired using a Slicescope upright microscope (Scientifica), with a 60x 1.0 numerical aperture (NA) objective, a multiple bandpass excitation/emission filter set (LED-DA/FI/TR/Cy5A, Semrock) and an ORCA-Flash4.0 CMOS camera (Hamamatsu) at 100 Hz and 2x2 pixel binning. Images were analyzed in ImageJ (NIH). For all Ca^{2+} imaging experiments and analyses, the experimenter was blind to the experimental condition.

Immunofluorescence of cultured neurons

Neuronal cultures at DIV14-16 were washed once with PBS and fixed with 4% paraformaldehyde in PBS for 10 minutes at RT. Cells were permeabilized in blocking solution containing 0.1% Triton X-100, 3% BSA in PBS, and incubated with primary antibodies against RIM (BD-Biosciences 610907, at 1:500 dilution for confocal microscopy, SySy 140 003, 1:500 for STED microscopy), synaptophysin (SySy 101 004, 1:500), vGAT (SySy 131 004, 1:500), Munc13-1 (SySy 126 103, 1:200), Bassoon (Enzo life sciences SAP7F407, 1:1000) and MAP-2 (Sysy 188 002, 1:1000) in blocking solution overnight at 4°C. Staining with AlexaFluor- or Oregon Green-coupled secondary antibodies (Life Technologies, 1:1000 for confocal microscopy, 1:200 for STED microscopy) was performed for 1 hr at room temperature (with isotype-specific secondary antibodies if necessary). Coverslips were air-dried at room temperature and mounted on to glass slides in mounting medium and stored at 4°C until imaging.

STED imaging and analysis

STED microscopy was performed as described in (Wong et al., 2018). Images were acquired with a Leica SP8 Confocal/STED 3X microscope with an oil immersion 100X 1.44 NA objective. 23.3 × 23.3 μm^2 synapse-rich areas were scanned at a sampling frequency of ~10 nm/pixel. Triple-color sequential confocal scans were followed by a dual-color sequential STED scans. Alexa 633, Alexa Fluor 555 and Oregon green 488 were excited with 633 nm, 555 nm and 488 nm white light lasers respectively at 2%–5%

of 1.5 mW laser power in this order of sequence. During STED scanning, Oregon green 488 and Alexa Fluor 555 signals were depleted with 592 nm (75% of max power) and 660 nm (25% of max power) time-gated depletion lasers. 4-times line accumulation and 3-times frame averaging were applied during STED scanning. Identical settings were applied to all samples within an experiment. In all STED experiments, vGAT was acquired in the confocal channel. To measure protein levels at active zones, masks that contained Bassoon signal within vGAT signals were created using MATLAB. These masks were used to measure fluorescence intensity of proteins in the second STED channel. For intensity profiles, side view vGAT positive synapses (Wong et al., 2018) were selected manually, and a rectangular 0.25 μm x 1.0 μm region of interest (ROI) was placed perpendicular to the Bassoon signals in ImageJ. Profiles were aligned on peak intensity of the Bassoon signal and in each channel normalized to the peak fluorescence in control. Note that for RIM and Munc13, peak localization relative to Bassoon is not always identical, and hence the average normalized control peak intensity is slightly below 1. All quantitative analyses were performed on original images without adjustments and were done identically for all experimental conditions. For all image acquisition the experimenter was blind to the experimental condition.

Confocal microscopy

Images were acquired at an Olympus FV1000 confocal microscope using a 60x 1.4 NA oil-immersion objective, and identical settings were applied to all samples within an experiment. Images were analyzed in ImageJ and MATLAB as described in (Wang et al., 2016). Synaptic levels of RIM were obtained by measuring RIM signal within synaptophysin puncta. 10 fields of view were quantified per culture per genotype. The experimenter was blind to the experimental condition of the culture.

Protein expression and purification

GST fusion proteins were expressed and purified according to standard procedures. The following proteins were produced: rat RIM1α C_2A (residues QVLPG….WYKLQ plasmids pAJ13026, pAJ14016, pGEX-KT RIM1 C_2A WT, pGEX-KT RIM1 C_2A WT R834, R835E and pGEX-KT RIM1 C_2A WT K809,R811E), RIM2 C_2A (residues QFLSG…WYKLQ, pAJ13027) RIM1α C_2B domain (residues GPAQL…PCIRS, (Guan et al., 2007), pAJ13005, pAJ13014, pGEX-KT RIM1 C_2B WT and pGEX-KT RIM1 C_2B K1513,K1515E), RIM2 C_2B domain (residues GPAQL…SYSRS, pAJ13028), RIM3-C_2B (residues GPAQI…SPSCS, pAJ15025), RIM4-C_2B (residues GPAQF…CGERS, pAJ15026), rat Liprin-α3-LH1 (residues CEVMP…LEEEL, pMYW12035), rat Liprin-α3-LH2 (residues ELSNQ…ELDGS, pMYW12036), and rat Syntaxin 1a (residues 2-253 KDRTQ…SDTKK, pGEX-KT Syntaxin1). In brief, fusion proteins were expressed at 25°C in *E. coli* BL21 (DE3) for 20 h with 0.5 mM isopropyl β-D-1-thiogalactopyranoside (IPTG), except GST-Liprin-α3-LH1 and -LH2, which were expressed at 18°C for 20 h with 50 μM IPTG. For GST-pulldown experiments, cells were resuspended in PBS, and lysed using lysozyme and brief sonication. Proteins were purified using glutathione-Sepharose resin in PBS and used within 5 days of purification.

For co-floatation assays, analytical ultracentrifugation and NMR spectroscopy, cells were resuspended in PBS buffer containing a protease inhibitor cocktail and lysed using an Avestin EmulsiFlex-C5 homogenizer. The RIM1α C_2A and C_2B domains were purified by the same procedure except that the RIM1α C_2B lysate was first treated with protamine sulfate (1% (w/v)) for 1 h at 4°C followed by centrifugation. The proteins were then isolated by affinity chromatography on glutathione-Sepharose. Resin was washed with PBS and PBS containing 1M NaCl. Remaining nucleic acid contaminants bound to the protein were then cleared with nuclease treatment (~600 units per liter of cell culture) in 50 mM Tris (pH 8.0), 2 mM $MgCl_2$ for 2 h at room temperature with gentle rotation of the beads. The GST tag was cleaved with thrombin on the resin at room temperature for 3 h. The eluted protein was further purified by size-exclusion chromatography on a Superdex 75 16/60 column using standard buffer (20 mM MES (pH 6.0), 150 mM NaCl, 1 mM EDTA, and 0.5 mM TCEP). Uniform ^{15}N-labeling was achieved by growing the bacteria in $^{15}NH_4Cl$ as the sole nitrogen sources.

Rat Syntaxin1A (residues 2-253) in pGEX-KT was expressed by induction with 0.4 mM IPTG at an OD_{600} of 1 at 25°C for 18 hours. Cells were resuspended in resuspension buffer (RB; PBS, 1mM EDTA, 5mM DTT and protease inhibitors). Cleared lysates were applied to glutathione Sepharose resin, washed with 100 mL RB, 200 mL RB + 1% Triton X-100, 200 mL RB + 1 M NaCl and 100 mL RB. The protein was then treated with nuclease for 1 hour at room temperature. The GST tag was removed by thrombin cleavage at 4°C overnight. The protein was further purified by ion exchange chromatography on a Source Q column using buffer A: 25 mM Tris pH 7.4, 1 mM TCEP and B: 25 mM Tris pH 7.4, 1M NaCl, 1mM TCEP. Source Q fractions (~38% NaCl) were frozen in liquid N_2 and stored at −80°C.

His-tagged RIM C_2A (pAJ14021 and pAJ14022) and C_2B proteins (pAJ13023, 14006, 14046, 14047, 16001-16008) were expressed using the same protocol as GST-fusion proteins. Proteins were isolated in 300 mM NaCl, 10 mM imidazole, 50 mM NaH_2PO_4 (pH 8.0) with Ni-NTA agarose and eluted from the resin in the same buffer containing 100-300 mM imidazole. After overnight dialysis to 150 mM NaCl, 25 mM HEPES (pH 8.0), aliquots were stored at −80°C until use. UV spectra were obtained on a Nanodrop 2000c (Thermo Fisher).

Human SNAP-25A full length in pET28A was expressed in E.coli BL21 (DE3) cells by induction with 0.4 mM IPTG at an OD_{600} of 0.8 at 23°C for 18 hours. Cells were resuspended in 50 mM Tris pH 8, 500 mM NaCl, 4 mM Imidazole, 1% Triton X-100, protease inhibitor. Cleared lysates were applied to Ni-NTA resin, washed with 100 mL resuspension buffer containing 20 mM Imidazole and treated with nuclease at 4°C overnight. The His-tag was removed by thrombin cleavage at room temperature for 1.5 hours. The protein was further purified by size exclusion chromatography on a Superdex S75 column (GE 16/60) equilibrated with 50 mM Tris pH 8, 150 mM NaCl. Fractions were concentrated to 50 μM, frozen in liquid N_2 and stored at −80°C.

Liposome co-sedimentation

Liposome co-sedimentation was performed essentially as described in (Shin et al., 2010). Porcine brain-derived lipids were obtained from Avanti Polar lipids: L-α-phosphatidylinositol-4,5-bisphosphate (PI(4,5)P_2), 1,2-dioleoyl-sn-glycero-3-phospho-(1'-myo-inositol-3′,4'-bisphosphate) (PI(3,4)P_2), 1,2-dioleoyl-sn-glycero-3-phospho-(1'-myo-inositol-3′,5′-bisphosphate) (PI(3,5)P_2), 1,2-dioleoyl-sn-glycero-3-phospho-(1'-myo-inositol-3′,4',5′-trisphosphate) (PI(3,4,5)P_3), L-α-phosphatidylserine (PS) and L-α-phosphatidylcholine (PC). Unless stated otherwise, the term PIP_2 refers to the PI(4,5)P_2 isomer. Lipids were mixed in glass tubes and dried under N_2, and resuspended in 100 mM NaCl, 25 mM HEPES (pH 8.0) and 500 mM sucrose by rigorous vortexing for 20 minutes and subsequent sonication to generate heavy liposomes. Buffer without sucrose was added to 12 mL, and liposomes were sedimented by ultracentrifugation at 150,000 x *g* for 30 min. The pellet was resuspended in buffer, and centrifuged again (20,800 x *g* 10 min). Liposome composition for each co-sedimentation experiment is indicated in the Figure legend. For binding assays, 200 μg liposomes were mixed with 10 μg protein in 1 mL buffer, and mixed for 10 minutes at 30°C while shaking at 10,000 RPM. Liposomes were pelleted for 10 min at 20,800 x *g* at 4°C, washed 3 times with buffer, and resuspended in 200 μL methanol:chloroform (2:1) and incubated for > 30 minutes at −20°C to solubilize the lipids and precipitate the proteins. Proteins were pelleted for 15 min at 20,800 x *g* at room temperature and resuspended in 30 μL 1X SDS sample buffer. Total recovered protein was assessed by SDS-PAGE with Coomassie staining, and quantified with densitometry in ImageJ. Background protein binding to the no lipids control was subtracted from all other samples.

Liposome preparation for co-floatation

Mixtures of 1,2-dioleoyl-sn-glycero-3-[phospho-L-serine] (PS), 1-palmitoyl-2-oleoyl-sn-glycero-3-phosphocholine (PC), 1,2-dipalmitoyl-sn-glycero-3-phosphoethanolamine-N-(lissamine rhodamine B sulfonyl) (PE), L-α-Phosphatidylinositol (PI), L-α-Phosphatidylinositol-4-phosphate (PIP) and L-α-Phosphatidylinositol-4,5-biphosphate (PIP_2) (Avanti Polar Lipids) were prepared by mixing the lipids dissolved in chloroform in a glass test tube in the desired ratio, and chloroform was evaporated using a dry nitrogen stream. The lipids were placed in a vacuum chamber overnight to remove organic solvent. Lipid films were hydrated with reconstitution buffer (25 mM HEPES pH 7.2, 150 mM NaCl) in an appropriate volume yielding 5 mM total lipid concentration. Lipids were vortexed > 5 min then frozen and thawed five times. Large unilamellar vesicles were prepared by extruding the hydrated lipid solution through 0.08-μm polycarbonate membranes 23 times using an Avanti Mini-Extruder. The homogeneity of the vesicle size distribution was confirmed by dynamic light scattering on a Wyatt DynaPro instrument (Wyatt Technology, Santa Barbara, CA).

Liposome co-floatation assays

Liposomes containing PC:PE(99:1), PC:PS:PE(84:15:1), PC:PS:PE:PI (83:15:1:1), PC:PS:PE:PIP (83:15:1:1) and PC:PS:PE:PIP_2 (83:15:1:1) were mixed with the proteins with a protein/lipid (P/L) ratio of 1:200 and incubated at room temperature for 1 hr. The liposomes and bound proteins were isolated by floatation on a Histodenz density gradient (40%:35%:30%) as described (Guan et al., 2008). Samples from the top of the gradient (35 μL) were taken and analyzed by SDS-PAGE and Coomassie blue staining.

NMR spectroscopy

All NMR data were acquired at 27°C on Varian INOVA600 spectrometers (Varian, Palo Alto, California, USA) with RIM1 C_2 domain samples dissolved in standard buffer (20 mM MES (pH 6.0), 150 mM NaCl, 1 mM EDTA, 0.5 mM TCEP), using H_2O/D_2O 95:5 (v/v) as the solvent. All 2D ^1H-^{15}N HSQC spectra testing phospholipid binding were acquired at 100 μM and 30 μM protein concentrations for C_2A and C_2B, respectively, and dibutanoyl phosphatidylinositol 4,5-bisphosphate (diC4-PIP_2) concentrations ranging from 5 to 300 μM. Spectra testing for SNARE protein binding were performed using 20 μM ^{15}N-labeled RIM1 C_2B and 25 μM unlabeled Syntaxin or SNAP-25. The 1D ^1H-NMR spectra were acquired with samples containing 100 μM RIM1α C_2B domain and in the presence or absence of 200 μM diC4-PIP_2. All 2D NMR spectra were processed with NMRPipe (Delaglio et al., 1995) and analyzed with NMRView (Johnson and Blevins, 1994). To derive K_D values from the diC4-PIP_2 titrations, the ^{15}N chemical shifts from selected cross-peaks, which were among those that had larger diC4-PIP_2-induced chemical shift changes and were better resolved, were plotted as a function of diC4-PIP_2 concentration. The data were then fitted to a standard single-site binding model using Sigma Plot.

Analytical ultracentrifugation

All centrifugation experiments were carried out in a Beckman-Coulter Optima XL-I (Beckman-Coulter, Brea, CA) at 20°C; a standard sedimentation velocity protocol was used (Zhao et al., 2013). The rotor speed was 50,000 rpm and the rotor was an An50-Ti (Beckman-Coulter, Brea, CA). A280 data were analyzed in SEDFIT using the c(s) distribution model (Schuck, 2000). The distributions were normalized, integrated, and rendered in GUSSI (Brautigam, 2015), and the resulting isotherm was examined in SEDPHAT (Schuck, 2003) to estimate the K_D, assuming and fixing the values of 1.85 S for the monomer and 3.1 S for the dimer.

GST pulldowns with His-tagged proteins

To test binding of C_2B domains to Liprin sequences, 6 μg GST- Liprin-α3-LH1 or -LH2 was mixed with 15 μg His-tagged RIM C_2B WT or mutant, in 100 mM NaCl, 25 mM HEPES (pH 7.4), 0.1% Triton X-100 and 1 mM DTT. After incubation for two hours at 4°C with gentle agitation, beads were washed 5 times with 500 μL buffer, and proteins were eluted from the beads with 1x SDS sample buffer. Binding was determined using Coomassie-stained 15% SDS-PAGE gels. Protein intensity was measured by densitometry

in ImageJ, and molar His-RIM C_2B to GST- Liprin-α3-LH was calculated by dividing both signals after correcting the raw signal for protein length.

GST pulldowns from mouse brain

To make brain lysate, brains from 6-10 week old wild-type mice were homogenized in 10 mL ice cold buffer containing 100 mM NaCl, 4 mM EGTA, 25 mM HEPES (pH 7.4) and protease inhibitor cocktail (Sigma, containing AEBSP, Aprotinin, Bestatin, E-64, Leupeptin and Pepstatin A), and incubated with 1% Triton X-100 for 1 hr. The insoluble fraction was removed by ultracentrifugation at 118,000 x *g* for 30 minutes. Supernatant was precleared from glutathione-binding proteins by incubation for 1 hr with 200 μL 50% glutathione-Sepharose beads. Subsequently, 15 μg GST-fusion protein was mixed with 1 mL cleared brain lysate, and incubated for 1 hr at 4°C with gentle agitation. To the $+Ca^{2+}$ pulldown conditions, 5 mM $CaCl_2$ was added to obtain $[Ca^{2+}]_{free}$ of 1 mM. Beads were washed 5 times with 1 mL buffer, and proteins were eluted from the beads with 100 μL 1X SDS sample buffer. Bound proteins were identified with SDS-PAGE and western blotting.

Western blotting

SDS-PAGE gels were transferred to nitrocellulose membranes (GE Healthcare) for 6.5 hr at 4°C in buffer containing (per L) 200 mL methanol, 14 g glycine and 6 g Tris. After blocking for 1 hr at RT in TBST with 10% non-fat milk powder and 5% normal goat serum (NGS), blots were stained for 2-3 hr at RT with primary antibodies in TBST with 5% milk and 2.5% NGS. Primary antibodies used were R809 (RIM1/2 PDZ and C_2A domains, (Schoch et al., 2002), 1:2000), HM1092 (RIM1/2 PDZ and C_2A domains, this study, 1:1000), U1130 (RIM1/2 c-terminus, (Schoch et al., 2002), 1:2000), 4396 (Liprin-α LH2 domain, (Schoch et al., 2002), 1:5000), V216 (synaptotagmin-1 cytoplasmatic domain, Südhof laboratory, 1:1000), P913 (SNAP-25, Südhof laboratory 1:2000), P939 (Synaptobrevin-2, Südhof laboratory, 1:2000), 438B (Syntaxin-1, Südhof laboratory, 1:1000), HA (Covance MMS-101P, 1:1000) and β-actin (Sigma A1978, 1:5000). After washing 5 × 5 min with TBST, blots were stained for 1 hr with horseradish peroxidase-conjugated secondary antibodies in the same solution, and blots were washed 5 × 5 min. Protein bands were visualized using enhanced chemiluminescence.

Antibody production

HM1092 RIM antibodies were raised in rabbit against a GST-fusion protein containing the PDZ domain an part of the C_2A domain of RIM1 (residues PGSAV…KVGHQ, identical to the immunogen of antibody R809, (Schoch et al., 2002), pAJ16009). The GST-fusion protein was purified as described above, and eluted from the beads with 10 mM glutathione for 3 hr at 4°C. After overnight dialysis to PBS, the protein was snap-frozen in ethanol/dry ice and submitted to Cocalico Biologicals for immunization using standard procedures. Sera were screened using western blots on protein samples from neuronal RIM1/2 control and RIM1/2 cDKO cultures. The serum with highest specific immunoreactivity (HM1092) for RIM was selected for use.

QUANTIFICATION AND STATISTICAL ANALYSIS

For electrophysiological and STED experiments, statistical differences were assessed using a one-way Kruskal-Wallis ANOVA with tukey-kramer correction for multiple testing, comparing against the cDKO condition. For PPR, a two-way ANOVA with tukey-kramer correction for multiple testing was used, testing genotype against cDKO. P values reported for one- and two-way ANOVAs are derived from the post hoc test as reported in each figure legend. For lipid co-sedimentation in Figures 3 and S3 and GST-pulldowns in Figure 6, a Student's t test was used. In all figures, * indicates $p < 0.05$, ** $p < 0.01$, and *** $p < 0.001$. No tests were used to estimate sample size. Except for NMR spectra and co-floatation assays, all experiments were performed at least 3 times to ensure reproducibility. The statistical tests used, the definition of n and the number of observations per experimental condition are specified in the figure legends. In all experiments, data is represented as mean ± standard error of the mean (SEM).

Neuron, Volume *98*

Supplemental Information

RIM C_2B Domains Target Presynaptic Active Zone Functions to PIP_2-Containing Membranes

Arthur P.H. de Jong, Carlos M. Roggero, Meng-Ru Ho, Man Yan Wong, Chad A. Brautigam, Josep Rizo, and Pascal S. Kaeser

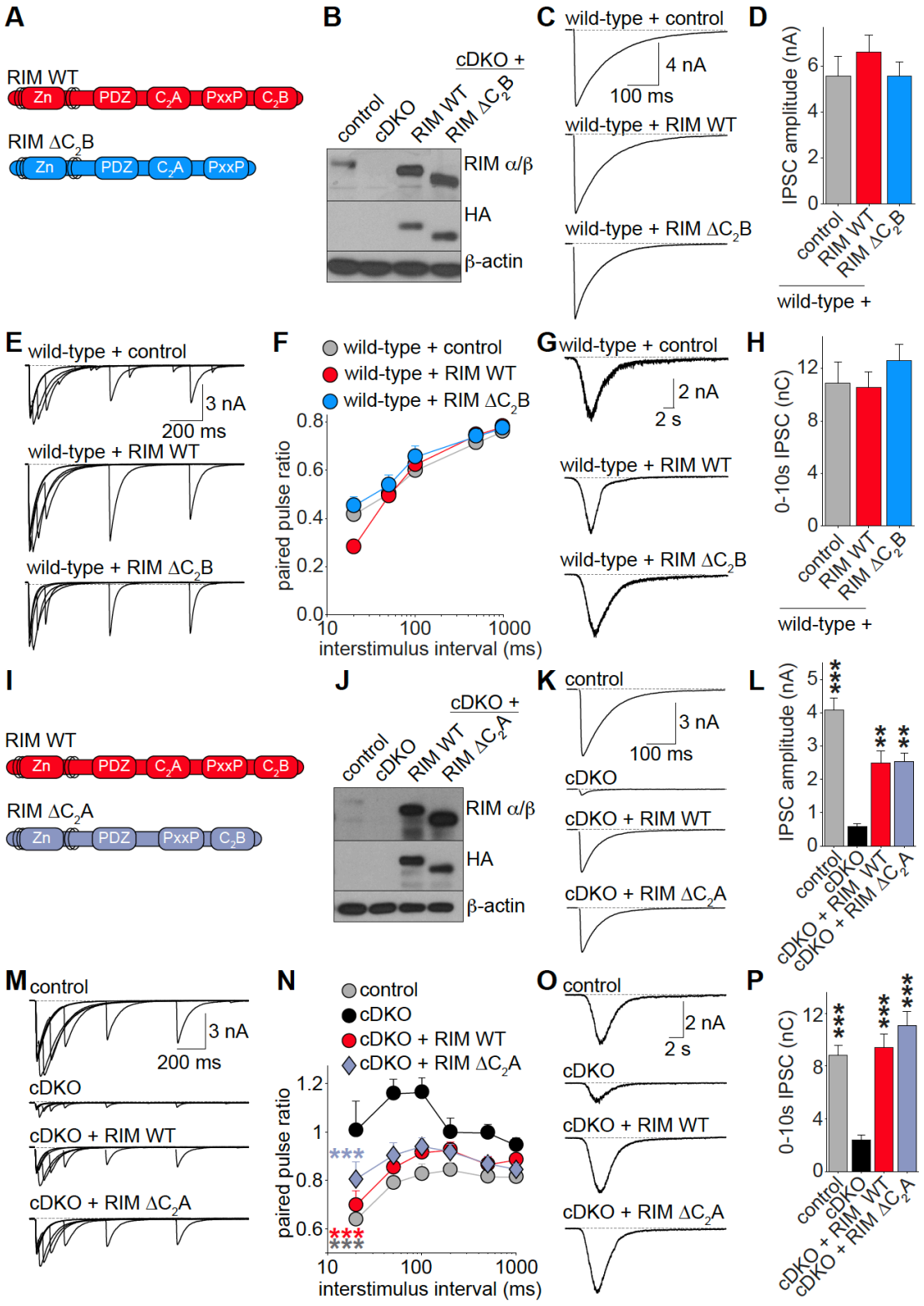

Figure S1, related to Figure 1. Expression of RIM ΔC_2B rescue, and effects of RIM ΔC_2B overexpression and RIM ΔC_2A rescue in wild-type neurons.

(A) Overview of rescue constructs.

(B) Representative western blots showing expression of RIM WT and RIM ΔC_2B in cDKO neuronal cultures. Antibody HM1092 was used for RIM.
(C, D) Example traces **(C)** and average amplitudes **(D)** of evoked IPSCs in wild-type neurons overexpressing RIM WT or RIM ΔC_2B delivered by lentiviral infection. Control cells were infected with a virus expressing inactive Cre. Control n = 2 independent cultures/10 cells, RIM WT 2/10, RIM ΔC_2B 2/10.
(E, F) Example traces **(E)** and average PPRs **(F)** of evoked IPSCs. Number of observations as in **(D)**.
(G, H) Example traces **(G)** and average integrated charge over 10 s **(H)** of IPSCs induced by a focal 10 s puff of hyperosmolar sucrose (500 mM) as a measurement of the RRP. Control n = 3 independent cultures/16 cells, RIM WT 3/15, ΔC_2B 3/16.
(I) Overview of rescue constructs.
(J) Representative western blot shown expression of RIM WT and RIM ΔC_2A in cDKO neuronal cultures. Antibody HM1092 was used for RIM.
(K, L) Example traces **(K)** and average amplitudes **(L)** of evoked IPSCs. Control n = 3 independent cultures/15 cells, cDKO 3/14, cDKO + RIM WT 3/14, cDKO + RIM ΔC_2A 3/12.
(M, N) Example traces **(M)** and average PPRs **(N)** at various inter-pulse intervals. Number of observations as in L.
(O, P) Example traces **(O)** and average integrated charge **(P)** of IPSCs induced by a focal 10 s puff of hyperosmolar sucrose (500 mM) as a measurement of the RRP. Control n = 3 independent cultures/14 cells, cDKO 3/15, cDKO + RIM WT 3/15, cDKO + RIM ΔC_2A 3/14.
All data shown as mean ± SEM, *p < 0.05, ** p < 0.01, *** p < 0.001 for IPSC amplitude analyzed by one-way ANOVA (Kruskal Wallis; **D**, **H**, **L**, and **P**), for PPR analyzed by two-way ANOVA **(F, N)**; all comparisons to cDKO.

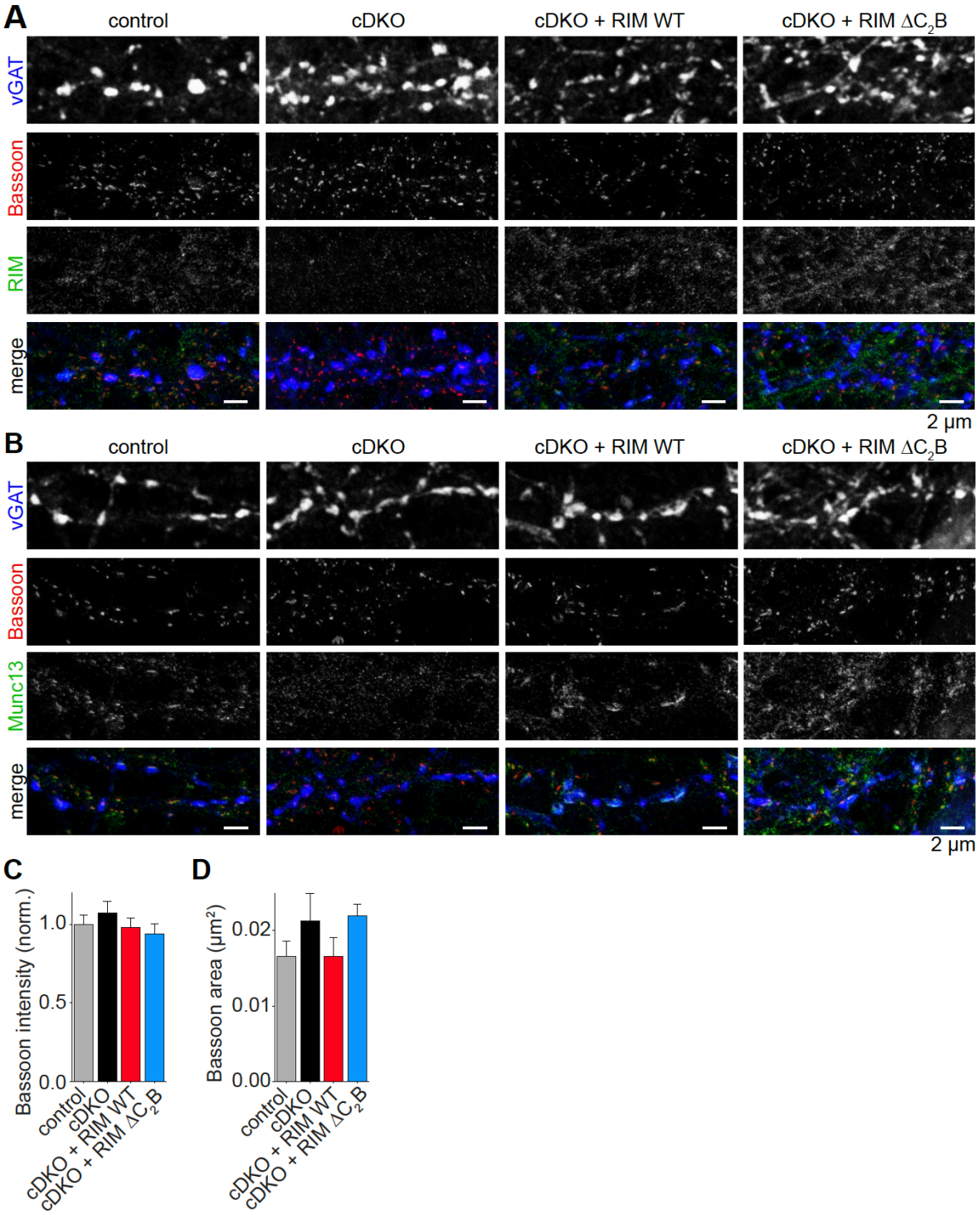

Figure S2, related to Figures 1 and 2. Localization of RIM and Munc13 in RIM ΔC_2B rescue experiments.

(A) Overview STED images of neuronal cultures stained for Bassoon, RIM and vGAT. Relates to Figures 1G-1M.

(B) Overview STED images of neuronal cultures stained for Bassoon, Munc13 and vGAT. Relates to Figures 2A-2D.

(C, D) Average intensity **(C)** and surface area **(D)** of Bassoon objects. Relates to STED analyses in Figures 2A-2D.
All data shown as mean ± SEM. Statistical difference analyzed by one-way ANOVA (Kruskal Wallis).

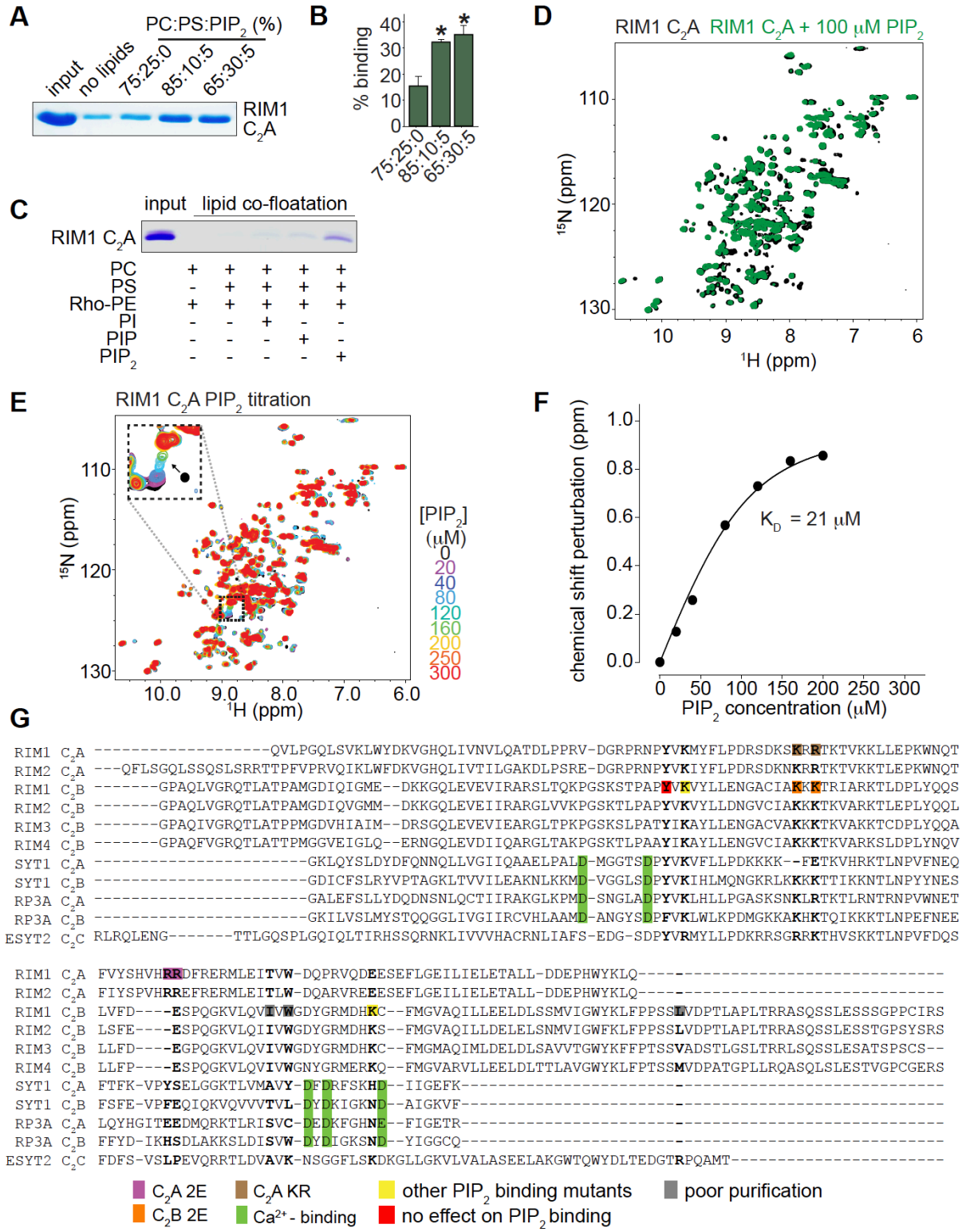

Figure S3, related to Figures 3 and 4. PIP_2 binding to RIM1 C_2A and alignment of C_2 domain sequences.

(A, B) Example images **(A)** and average binding **(B)** of lipid co-sedimentation experiments to test PIP_2 binding of C_2A. Average data was obtained from 3 independent experiments and statistical

significance was tested using a Students *t* test against 75:25:0 %.

(C) Image of a stained SDS-PAGE gel of a lipid co-floatation assay with RIM1 C_2A to test for PIP_2 specificity of lipid-C_2A binding. The assay was performed with GST-purified RIM1 C_2A and liposomes containing different lipids, as indicated. The liposome fractions were analyzed by SDS-PAGE and Coomassie blue staining.

(D) Analysis of PIP_2 binding to RIM1 C_2A using NMR spectroscopy. Superposition of ^{1}H-^{15}N HSQC spectra of ^{15}N-labeled RIM1 C_2A alone (black contours) and in the presence of 100 µM diC4-PIP_2 (green contours).

(E) Superposition of ^{1}H-^{15}N HSQC spectra of RIM1 C_2A acquired in the presence of different diC4-PIP_2 concentrations as indicated by the color code. The black circle indicates the cross-peak shift for which the dissociation constant (K_D) was calculated, as shown in panel F.

(F) Analysis of the binding affinity of PIP_2 to ^{15}N-labeled RIM1 C_2A using NMR spectroscopy. Plot of the ^{15}N chemical shift perturbation of the cross-peak of the residue marked with a black circle in E as a function of diC4-PIP_2 concentration. The data were fitted with a standard single-site binding model, yielding the K_D.

(G) Sequence alignment of the C_2A and C_2B domains of rat RIM1 (Uniprot ID Q9JIR4), RIM2 (Q9JIS1), RIM3 (Q9JIR3), RIM4 (Q8CIX1), synaptotagmin-1 (SYT, P21707), rabphilin 3A (RP3a, P477709) and C_2C of human extended synaptotagmin-2 (ESYT2, A0FGR8). All mutants used throughout the manuscript, and their observed effects, are color coded. Residues known to bind Ca^{2+} in synaptotagmin-1 and Rabphilin 3a are indicated as well. Conservation of mutated residues is indicated in bold.

Data in **B** are shown as mean ± SEM, *p < 0.05.

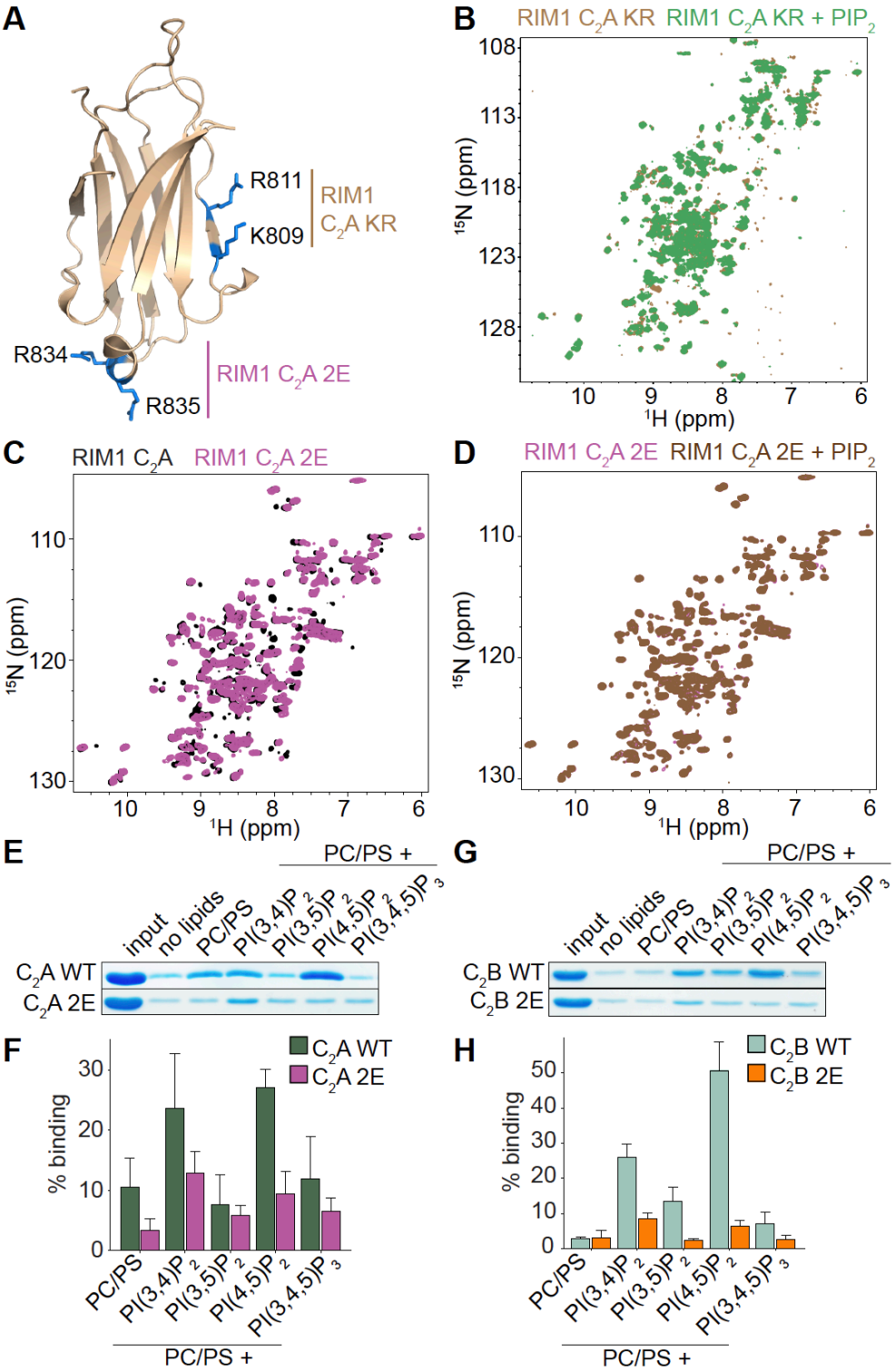

Figure S4, related to Figure 4. Mutational analyses of RIM C_2A PIP_2 binding and PIP_2 isomer specificity of C_2B.

(A) Ribbon diagram of the RIM2 C_2A domain (PDB: 2BWQ, (Dai et al., 2005)). Mutated residues in C_2A 2E (R834, R835) and C_2A KR (K809, R811) are highlighted in blue.

(B) Superposition of ^{1}H-^{15}N HSQC spectra of ^{15}N-labeled RIM1 C_2A KR (brown contours) and

RIM1 C_2A KR in the presence of 100 µM diC4-PIP_2 (green contours).
(C) Superposition of ^{1}H-^{15}N HSQC spectra of ^{15}N-labeled RIM1 C_2A WT (black contours) and RIM1 C_2A 2E (purple contours) domains.
(D) Analysis of the PIP_2 binding to ^{15}N-labeled RIM1 C_2A 2E using NMR spectroscopy. Superposition of ^{1}H-^{15}N HSQC spectra of RIM1 C_2A 2E alone (purple contours) and RIM1 C_2A 2E in the presence of 100 µM diC4-PIP_2 (brown contours) reveal that no cross peak shifts occur upon addition of diC4-PIP_2, indicating that PIP_2 binding is abolished in the 2E mutant.
(E, F) Example images **(E)** and average binding **(F)** of C_2A to PIP_3 and various PIP_2 isomers in co-sedimentation experiments. Co-sedimentation was performed with liposomes of identical surface charge. Liposome composition (PC:PS:PIP_x) : PC/PS 75:25:0, PC/PS + PI(x,x)P_2 85:10:5, PC/PS + PI(3,4,5)P_3 95:0:5. Average binding was obtained from 3 independent experiments.
(G, H) Same analysis as in panels **E** and **F**, but using C_2B WT and C_2B 2E.
Data are shown as average ± SEM.

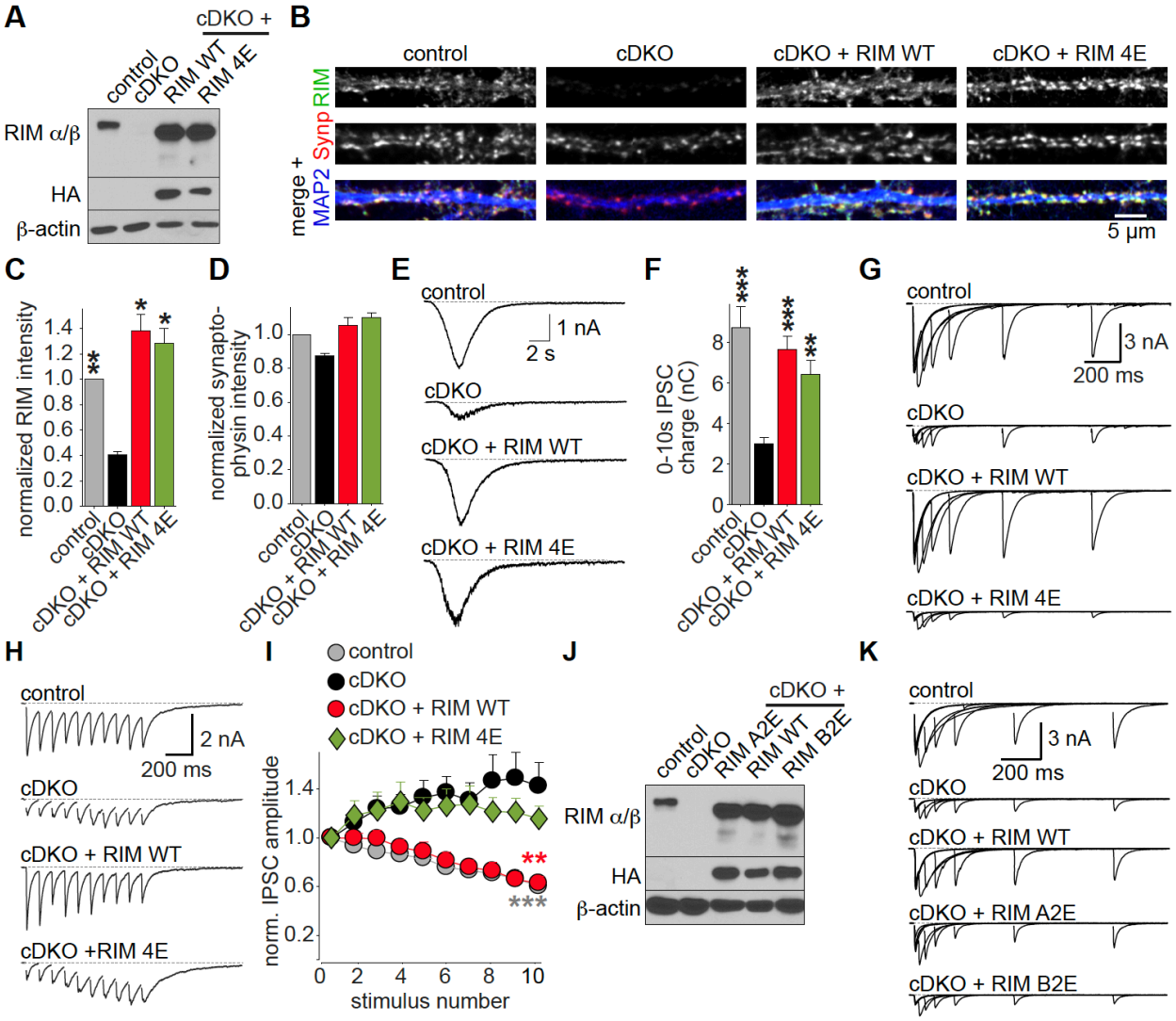

Figure S5, related to Figure 5. Expression, localization and electrophysiological analyses of various RIM PIP_2 binding mutants.

(A) Example western blots showing expression of RIM WT and RIM 4E in cDKO neuronal cultures. RIM R809 antibodies were used to detect RIM.

(B-D) Representative confocal images **(B)** and quantification **(C, D)** of neuronal cultures stained for MAP2, RIM and Synaptophysin. Average RIM intensity within synaptophysin puncta **(C)** and synaptophysin intensity **(D)** are shown. Values were normalized for every culture to control. Scale bar in **(B)** applies to all images. Control n = 3 independent cultures/28 images, cDKO 3/29, cDKO + RIM WT 3/31, cDKO + RIM 4E 3/29. Statistical difference was assessed by paired t-test.

(E, F) Example traces **(E)** and average integrated charge over 10 s **(F)** of IPSCs induced by a focal 10 s puff of hyperosmolar sucrose (500 mM) as a measurement of the RRP. Control n = 3 independent cultures/19 cells, cDKO 3/18, cDKO + RIM WT 3/19, cDKO + RIM 4E 3/20. Statistical difference was assessed by one-way ANOVA (Kruskal-Wallis).

(G) Example traces of PPRs. Relates to Figure 5D.

(H, I) Example traces **(H)**, and normalized amplitude **(I)** of IPSCs evoked by 10 stimuli at 10 Hz. Control n = 5 cultures/20 cells, cDKO 5/17, cDKO + RIM WT 5/23, cDKO + RIM 4E 5/21. Statistical

difference was assessed by two-way ANOVA comparing genotypes.
(J) Example western blots showing expression of RIM A2E, RIM WT and RIM B2E in cDKO neuronal cultures, RIM R809 antibodies were used to detect RIM.
(K) Example traces of PPRs. Relates to Figure 5H.
All data shown as average ± SEM, statistical tests performed as indicated vs cDKO with * $p < 0.05$, ** p 0.01, *** $p < 0.001$.

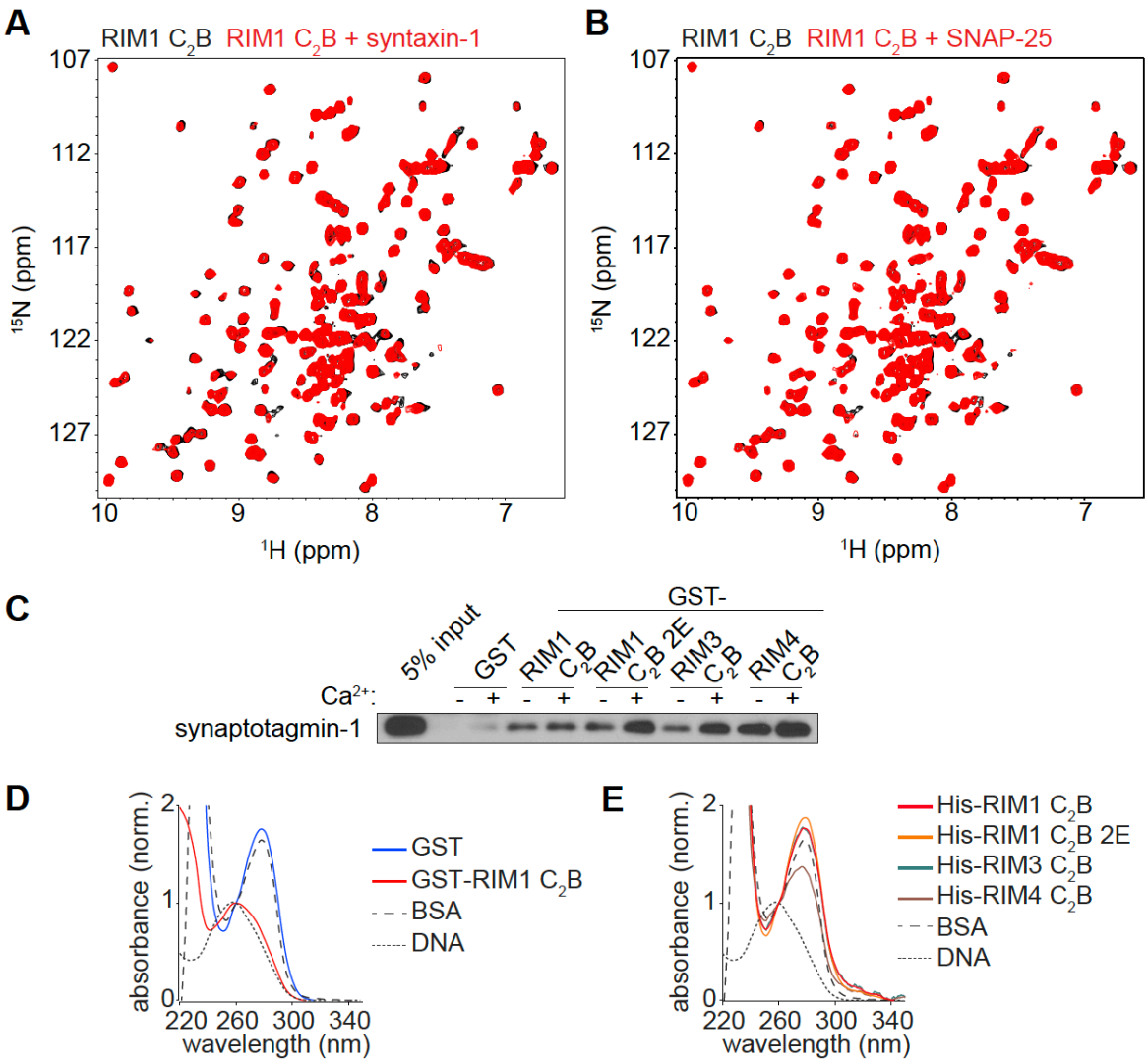

Figure S6, related to Figure 6. Analyses of SNARE and synaptotagmin-1 binding to C_2B.
(A, B) Superposition of ^{1}H ^{15}N HSQC spectra of 100 µM ^{15}N labeled RIM1 C_2B WT without (black contours) and with (red contours) 100 µM unlabeled cytoplasmic region of syntaxin-1 (residues 2-253) **(A)** or full-length SNAP-25 **(B)**.
(C) Example images of western blot of in vitro binding assays to test for Ca^{2+}-dependent binding to synaptotagmin-1. The $+Ca^{2+}$ condition contained 1 mM free Ca^{2+}. Note that, although this reproduces previous findings (Coppola et al., 2001; Schoch et al., 2002), C_2 domain homo- and heterodimerization experiments are sensitive to contaminants, including bacterial DNA, from standard GST-purification protocols (Ubach et al., 2001 and panel **D** below). The binding to synaptotagmin-1 observed here is most likely due to these contaminants. C_2-C_2 domain interactions, including binding of RIM1 C_2B to synaptotagmin-1 C_2B and homodimerization of synaptotagmin-1 via a similar binding mode, could previously not be observed using highly purified protein preparations where these contaminants were removed (Guan et al., 2007; Ubach et al., 2001).
(D) UV spectra of GST and GST-RIM1 C_2B, demonstrating the presence of DNA contaminants in GST-RIM1 C_2B after affinity purification. Bovine serum albumin (BSA) and plasmid DNA are

shown for comparison. For NMR, analytical ultracentrifugation and co-floatation experiments in Figures 3, 4, S3, S4 and S6, additional purification steps were performed to remove these contaminants (see methods). All traces are an average of 3 measurements; traces are normalized to absorbance at 260 nm.

(E) UV spectra of His-RIM C_2B proteins, establishing that the His-tag purification protocol used here largely eliminates DNA-contaminants. All traces are an average of 3 measurements; traces are normalized to absorbance at 260 nm. BSA and DNA traces are identical to panel **D**.

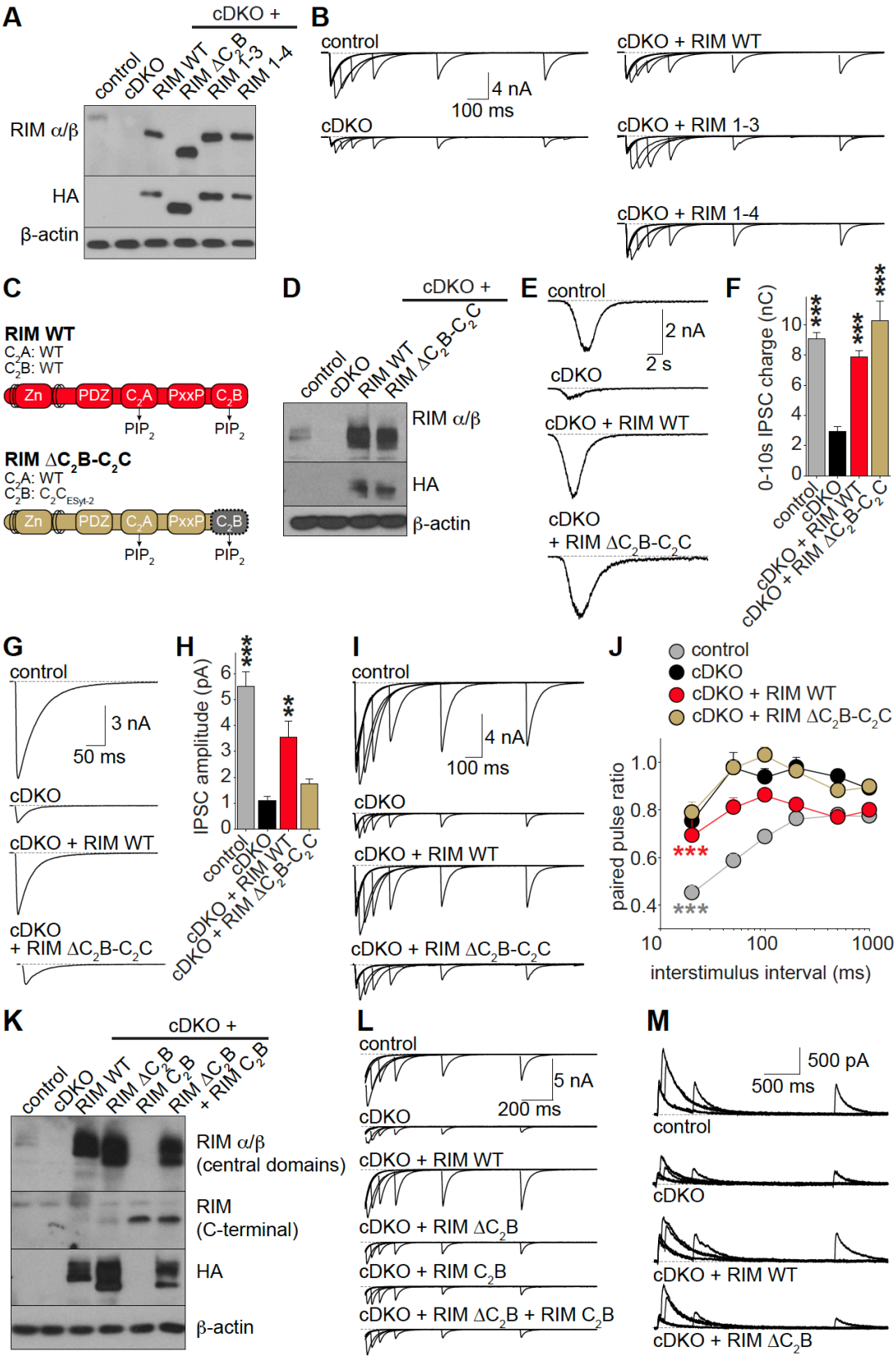

Figure S7, related to Figures 6 and 7. Analyses of expression of RIM1-3 and RIM1-4 and

electrophysiological analyses of RIM ΔC_2B-C_2C (A-J, related to Figure 6), and expression analysis of RIM ΔC_2B + RIM C_2B and example traces of paired pulse experiments (K-M, related to Figure 7).

(A) Example western blots showing expression of RIM WT, RIM ΔC_2B, RIM 1-3 and RIM 1-4 in neuronal cultures. RIM R809 antibodies were used for detection of RIM.

(B) Example traces of PPRs. Relates to Figure 6I.

(C) Overview of rescue constructs.

(D) Example western blots showing expression of RIM ΔC_2B-C_2C in neuronal cultures. Antibody HM1092 was used for RIM.

(E, F) Example traces **(E)** and integrated charge over 10 s **(F)** of IPSCs induced by a focal 10 s puff of hyperosmolar sucrose (500 mM) as a measurement of the RRP. Control n = 3 independent cultures/13 cells, cDKO 3/13, cDKO + RIM WT 3/13, cDKO + RIM ΔC_2B-C_2C 3/12.

(G, H) Example traces **(G)** and average amplitude **(H)** of evoked IPSCs. Control n = 3 independent cultures/14 cells, cDKO 3/14, cDKO + RIM WT 3/13, cDKO + RIM ΔC_2B-C_2C 3/14.

(I, J) Example traces **(I)** and average PPRs **(J)** at various inter-pulse intervals. Number of observations as in H.

(K) Example western blots showing expression of RIM WT, RIM ΔC_2B and RIM C_2B in neuronal cultures. In the RIM ΔC_2B + RIM C_2B, RIM ΔC_2B was expressed from one lentivirus, and cre-recombinase and RIM C_2B were expressed by a second lentivirus in which Cre was followed by a 2A peptide and RIM C_2B. Antibody HM1092 was used to detect RIM central domains, U1130 to detect the RIM C-terminus. Relates to Figures 7A-7D.

(L) Example traces of IPSC PPRs at various inter-stimulus intervals. Relates to Figure 7D.

(M) Example traces of NMDA receptor EPSC PPRs at various inter-stimulus intervals. Relates to Figure 7G.

All data shown as mean ± SEM, *$p < 0.05$, ** $p < 0.01$, *** $p < 0.001$ for IPSC amplitude analyzed by one-way ANOVA (Kruskal Wallis; **F**, **H**), for PPR analyzed by two-way ANOVA **(J)**; all comparisons to cDKO.